Energy & Environmental Science

ROYAL SOCIETY OF CHEMISTRY

REVIEW

View Article Online
View Journal | View Issue

Cite this: *Energy Environ. Sci.*, 2020, **13**, 404

Towards the commercialization of colloidal quantum dot solar cells: perspectives on device structures and manufacturing

Hyunho Lee, †[a] Hyung-Jun Song, †[b] Moonsub Shim *[a] and Changhee Lee *[c]

Received 17th October 2019,
Accepted 3rd January 2020

DOI: 10.1039/c9ee03348c

rsc.li/ees

Over the past decade, colloidal quantum dot solar cells (CQD-SCs) have been developed rapidly, with their performances reaching over 16% power conversion efficiency. Accompanied by the development in materials engineering (CQD surface chemistry) and device physics (structures and defect engineering), CQD-SCs are moving towards commercialization. A broad overview of the requirements for commercialization is thus timely and imperative. Broad comprehension of structure engineering, upscaling techniques, stability and the manufacturing cost of CQD-SCs is necessary and should be established. In this review, the development of device structures is presented with their corresponding charge transfer mechanisms. Then, we overview the upscaling methods for the mass production of CQD-SCs. Comparisons between each of the upscaling techniques suggest the most advanced process close to industrialization. In addition, we have investigated the origin of the photovoltaic (PV) performance degradation. The possible degradation sources are categorized according to external environmental factors. Moreover, strategies for improving the stability of CQD-SCs are presented. In the conclusion, we have reviewed the cost-effectiveness of CQD-SCs in terms of the niche PV market. Step-wise manufacturing cost analysis for the commercial CQD-SCs is presented. In the conclusion, the future direction for environment-friendly CQD-SCs is discussed.

Broader context

Colloidal quantum dots (CQDs) have received growing attention with respect to solar energy harvesting systems on account of the possibility of using them for multi exciton generation, and their ease of energy level control, and solution-based processing. The efficiencies of CQD solar cells have increased rapidly and reached over 16%. It is expected that CQD solar cells will enter a market for non-utility scale, portable, and flexible applications. By utilizing their wide range (~1400 nm) light absorbance characteristics, CQD solar cells can convert low energy infrared light into electricity, which is barely harvested by conventional crystalline silicon solar cells or other emerging photovoltaics. Moreover, adding a stack of low band gap CQD solar cells to conventional (crystalline silicon) photovoltaic systems, in so-called tandem structures, could boost their efficiency by converting low energy IR light into electricity. This review aims to provide a comprehensive summary of the current status of CQD solar cells from the viewpoint of the progress in terms of performance and the development of the device structure. In addition, the key issues surrounding CQD solar cells for realizing large-sized stable devices are addressed. Moreover, opportunities and challenges for marketability and mass production will be discussed.

1. Introduction

Colloidal quantum dots (CQDs) are chemically synthesized semiconductor nanocrystals with sizes of typically less than 10 nm. Because of the quantum confinement effect in CQDs, their electrical and optical properties can be easily tuned by modifying their shape and size, which is difficult to achieve in bulk materials.[1] Thus, CQDs have drawn much attention as a highly flexible platform for realizing next-generation optoelectronic devices. Moreover, solution-processed CQDs allow the fabrication of devices *via* a roll-to-roll process, thereby

[a] *Department of Materials Science and Engineering, Frederick Seitz Materials Research Laboratory, University of Illinois at Urbana-Champaign, Urbana, IL 61801, USA. E-mail: mshim@illinois.edu*
[b] *Department of Safety Engineering, Seoul National University of Science and Technology, Seoul 01811, Republic of Korea*
[c] *Department of Electrical and Computer Engineering, Inter-University Semiconductor Research Center, Seoul National University, Seoul, 08826, Republic of Korea. E-mail: chlee7@snu.ac.kr*
† Hyunho Lee and Hyung-Jun Song contributed equally to this work

decreasing the manufacturing cost.[2] Consequently, over the last two decades, significant progress has been achieved in the area of CQD-based optoelectronic devices, including light-emitting diodes (LEDs), field-effect transistors (FETs), and photodiodes.[3] Currently, CQD-incorporated LEDs compete with other devices in the high-end display market.[4] Other applications for the development of highly-efficient and commercially-available devices have also been intensively studied.

CQD solar cells (CQD-SCs) have very promising applications. First, these SCs can be fabricated on flexible plastic substrates using a solution-based approach. In addition, CQD films meet the requirements for efficient solar energy harvesting systems in terms of their optical and electrical properties. As the absorption coefficients of CQDs are $\sim 10^6$ cm^{-1}, a film of only a few hundred nanometres is sufficiently thick enough to absorb sunlight in the range of the CQD bandgap (E_g).[5] Moreover, the E_g of a CQD can be easily tuned by varying its size and shape, to achieve the desired value. Thus, a broad spectral range can be harnessed in CQD-based SCs. Furthermore, such cells have the potential to be utilized in tandem devices, incorporating other CQDs and/or thin-film SCs. In particular, large-sized CQDs can convert IR light into electricity, which is suitable for the bottom cell of a tandem structure. Regarding the electrical characteristics, the carrier mobility of a well-prepared CQD film exceeds 1 cm^2 V^{-1} s^{-1}, which allows the photogenerated carriers to be transported to the electrode with only small losses.[6,7] Additionally, preferentially oriented carrier transport can be achieved in anisotropic nanostructures, such as nanorods and tetrapods.[8–10] Also, the energy levels of a CQD can be modified by controlling its surface treatment.[11,12] Different from other bulk semiconductor materials, in CQD films, hot carrier extraction is possible *via* multiple exciton generation (MEG). Owing to the quantum confinement in a CQD, its efficiency of MEG, in which two excitons are generated from one absorbed high energy photon, is higher than that in bulk semiconductors.[13] Empirically, the external quantum efficiency (EQE) of PbS CQDs has been reported to exceed 100% in the blue and UV regions.[14] Thus, CQD-SCs are expected to be a platform to overcome the

Hyunho Lee

Hyunho Lee received his BS degree from the Korea Advanced Institute of Science and Technology (KAIST, Electrical Engineering) in 2013. He completed his PhD at Seoul National University (Electrical and Computer Engineering) under the supervision of Prof. Changhee Lee in 2018. Currently, Hyunho Lee is a postdoctoral research associate at the University of Illinois at Urbana-Champaign.

Hyung-Jun Song

Hyung-Jun Song earned his BS and PhD degrees in Electrical Engineering from Seoul National University in South Korea. After finishing a postdoctoral program in the nanotechnology and advance spectroscopy team at Los Alamos National Laboratory (USA), he is currently working at Seoul National University of Science and Technology as an associate professor. His research focuses on developing highly efficient and reliable photovoltaic devices and systems.

Moonsub Shim

Moonsub Shim is a professor of Materials Science and Engineering at the University of Illinois at Urbana-Champaign. He received his BS degree from the University of California at Berkeley in 1997 and his MS and PhD degrees both from the University of Chicago in 1998 and 2001. After working as a postdoctoral researcher at Stanford University, he joined the faculty of the Department of Materials Science and Engineering at Illinois in 2002. His research interests revolve around nanoscale materials, spanning materials synthesis to charging and charge-separation processes to their applications in electronics, optoelectronics, and photovoltaics.

Changhee Lee

Changhee Lee received his BS and MS degrees from Seoul National University in 1987 and 1989 and his PhD degree from the University of California at Santa Barbara in 1994. After working as a Senior Scientist at LG Chem. (1994–1997), an associate professor of Physics at Inha University (1997–2004) and a professor of Electrical Engineering at Seoul National University (2004–2018), he became an Executive Vice President of Samsung Display Co., where he is developing next-generation display technologies. He is a SID Fellow and a member of the Korean Academy of Science and Technology and the National Academy of Engineering of Korea.

Shockley–Queisser limit of a single cell.[15] By exploiting the excellent optical and electrical properties of CQDs, the certified power conversion efficiencies (PCE) of CQD-SCs have recently exceeded 16%.

Many materials and compounds have been suggested as solar energy harvesting CQDs. Originally, II–VI CQDs with toxic Cd (CdSe, CdTe and CdS) were adopted in SCs. However, the E_g values of these CQDs are large, so their absorption spectrum can only cover the visible light range (up to 800 nm). To utilize a wide solar spectral range extending to the infrared (IR) region, many non-toxic binary (InAs, InP) and ternary ($AgBi_2S$, $CuInS_2$, $CuInSe_2$)-based nanocrystals have been introduced into SCs.[16] Since the bulk films of these compounds exhibit excellent photovoltaic (PV) properties, highly efficient devices are expected to be fabricated when employing these non-toxic CQDs within them. However, the device efficiencies of these CQD-SCs are not very high because of the poor understanding of their energy levels, poor size control, and lack of a good synthesis method to produce them. To date, most record high results have been obtained from SCs with PbS and PbSe nanocrystals, which absorb in a broad range of the solar spectrum, from UV to IR.

Fig. 1 shows the development of the PCE of the CQD-SCs (Pb-based) and the number of publications over time. Over two thousand studies have been reported since 2008, contributing to the improvement of the PCE over the past decade. The field of CQD-SCs is now moving towards their commercialization with the featured advantages of CQDs. Although intensive studies have been conducted to improve the efficiency and stability of CQD-SCs, they are still lab-scale and prototype devices compared to other types of solar cells. According to a market survey by the Fraunhofer Institute of Solae Energy (ISE, Germany) and the National Renewable Energy Laboratory (NREL, United States), the annual installation of photovoltaic systems exceeded 90 GW in 2018. Among the many types of cells, crystalline silicon (C-Si) and other thin film-based cells (CdTe, Cu–In–Ga–Se, amorphous Si and GaAs) are competing in the PV market, and their manufacturing facilities are already over the GW scale (please see Fig. 2).[17,18] On the other hand, other emerging technologies, including CQDs, perovskites, organics and so on, are still being used to enhance the performance of prototype devices. Currently, only a few companies (*e.g.* QD solar, Quantum materials corp.) aim to demonstrate commercially available CQD-SCs, while others (*e.g.* Nanosys, Nanoco, QD vision and so on) focus on improving the electrical and optical properties of QDs. Nevertheless, as the performance of CQD-SCs has been enhanced significantly over the last decade, it is expected that they will enter the flexible solar cell market very soon. To occupy a proper PV market share, several issues should be addressed, such as efficiency, mass production of device structures, manufacturing processes, device stability and cost effectiveness of the materials, as well as fabrication. Although progress and research trends in CQD-SCs have been clearly summarized in other review

Table 1 The PCE development of CQD-SCs

Published year	PCE (%)	Reference (type of active layer)
2008	2.1	PbSe[19]
2009	3.4	PbSe[20]
2010	2.9–5.1	PbS[21–23]
2011	5.1–5.7	PbS[24–27]
2012	5.4–7.4	PbS[28–31]
2013	7.3–8.4	PbS[32–34]
2014	6.1–8.6	PbS[35–38]
2015	7.3–9.0	PbS[39–41]
2016	9.0–10.6	PbS,[12,42–46] $CsPbI_3$[47]
2017	10.4–11.6	PbS,[48–53] $CsPbI_3$[54]
2018	10.6–12.5	PbS,[2,55–62] $CsPbI_3$[63,64]
2019	10.4–16.6	PbS,[65] $CsPbI_3$,[66,67] *etc.*[18]

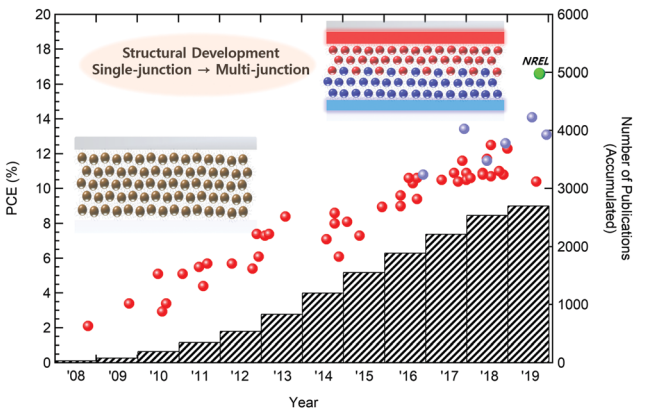

Fig. 1 PCE development of CQD-SCs based on the accumulated number of publications over the years. Each plot of the PCE is based on Table 1. The red dots represent PbS- and PbSe-based CQD-SCs. The sky-blue dots represent $CsPbI_3$ CQD-SCs. The green dot represents the PCE record held by the National Renewable Energy Laboratory (NREL). The type of active layer has not been reported. The plot data is taken from the Web of Science, found by searching for quantum dot solar cells and colloidal quantum dot solar cells.

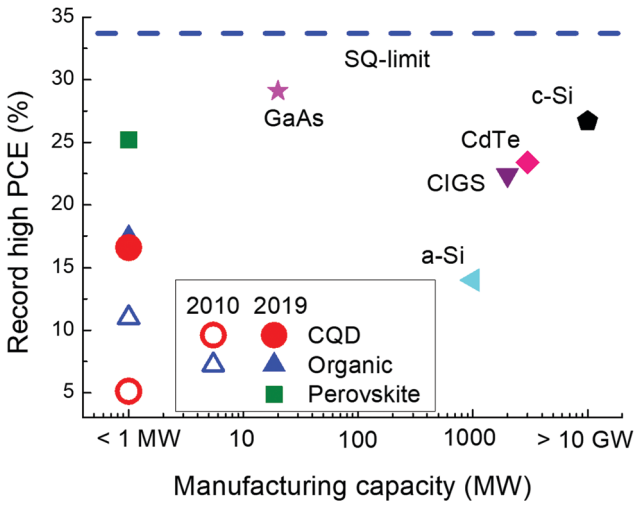

Fig. 2 Record high efficiency and manufacturing capacity of various type of photovoltaic cells. Five technologies, based on c-Si, CdTe, Cu–In–Ga–Se (CIGS), amorphous silicon (a-Si), and GaAs, compete with each other in the market, while other emerging solar cells are still prototype devices. However, the efficiencies of emerging solar cells have increased rapidly over ten years, so it is expected that they will enter the commercial market sometime in the near future.

papers, the approach of the commercialization of CQD-SCs has been barely addressed. Considering the progress in CQD-SCs, it would be fruitful to figure out the current status of CQD-SC technologies and their possible commercialization for further future studies. In this review, we cover the progress in CQD-SCs towards commercialization. First, the device physics will be discussed to determine the most efficient device structures and device engineering methods to date. Then, we will discuss the viability of upscaling the manufacturing of CQD-SCs for mass production. Furthermore, progress on the stability of the devices will be reviewed along with degradation mechanisms involving internal or external degradation sources. Finally, the possible approaches towards the commercialization of CQD-SCs will be reviewed in terms of cost considerations and environmental issues.

2. Device physics

2.1 Device structures

The device structure is the most important factor that affects charge generation and transport in CQD-SCs. Device structures have been developed to extend the depletion region in the CQD layer and optimize the energy level alignment for efficient charge extraction to the electrodes. This section addresses the development of device structures in terms of charge generation, transport mechanisms, and ultimately, PV performance.

2.1.1 Schottky CQD-SCs. Schottky CQD-SCs were the first proposed device structure, in which the CQD active layer is sandwiched between a transparent electrode (ITO (indium tin oxide) or FTO (fluorine-doped tin oxide)) and a counter metal electrode. n-Type or p-type CQD films form Schottky junctions with counter metal electrodes (Fig. 3(a)). A potential difference at the junction leads to the charge extraction of photogenerated carriers from the CQD layer to each electrode. In theory, the height of the Schottky barrier is estimated by the difference in the work functions of each electrode (Fig. 4(a)). However, experimental results have shown that the barrier heights are normally less than the difference in the work functions of each electrode.[68] The E_g of a CQD changes depending on the size of the nanocrystals. The E_g energy increases as the nanocrystal diameter decreases. The shorter first excitation wavelength of smaller CQDs results in an improvement in open circuit voltage (V_{OC}). The work function difference between metal electrodes (Ca, Mg, Ag, Al and Au) results in different V_{OC} values as well as different Schottky barriers, as shown in Fig. 4(b).[19] Thickness control of a ligand-exchanged CQD layer has been shown to enable improvement in the PV performance, achieving a 5.2% PCE.[69] In addition, CQD layers have been oxidized to enlarge the Schottky barrier height *via* air annealing and UV-ozone treatment. An oxidized PbS film induces a hole injection barrier that leads to a built-in voltage improvement.[70] Moreover, insertion of a buffer layer between the electrodes and CQD layer provides an increased energy barrier, thereby resulting in better carrier transport. A thin LiF layer has been applied to enhance the Schottky barrier stability at the interface between the CQD layer and metal electrode.[71] The work function of FTO was tuned *via* the insertion of polyelectrolyte (polyethylenimine, PEI), increasing the Schottky junction barrier at the CQD/FTO interface.[72] Nevertheless, the limitation on the Schottky barrier height tuning and the weak stability of the Schottky junction of the CQDs mitigate the advantages of the easy fabrication process and simple device structure of Schottky CQD-SCs. To date, the reported V_{OC} values of Schottky CQD-SCs are far below the expected V_{OC} values based on the E_g values of CQDs. Nevertheless, Schottky CQD-SC structures are efficient tools for investigating the material characteristics, such as carrier mobility, diffusion lengths, and doping concentrations of CQD films.[12]

2.1.2 Depleted heterojunction CQD-SCs. The development of depleted heterojunction CQD-SCs is inspired by p-i-n-based PV devices. CQD layers are deposited on top of oxides with wide E_g values (TiO_2 or ZnO), forming junctions with the electron transport layers (ETLs). The introduction of a junction between

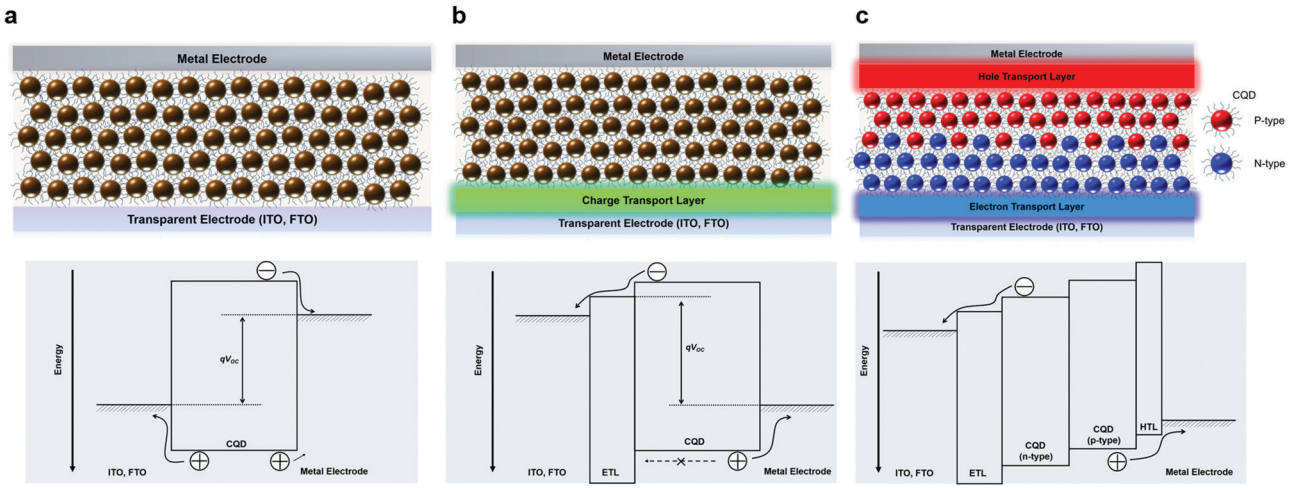

Fig. 3 Schematic diagram of device structures and their energy level bands. (a) Schottky CQD-SCs. (b) Depleted heterojunction CQD-SCs. (c) Quantum junction or band alignment CQD-SCs.

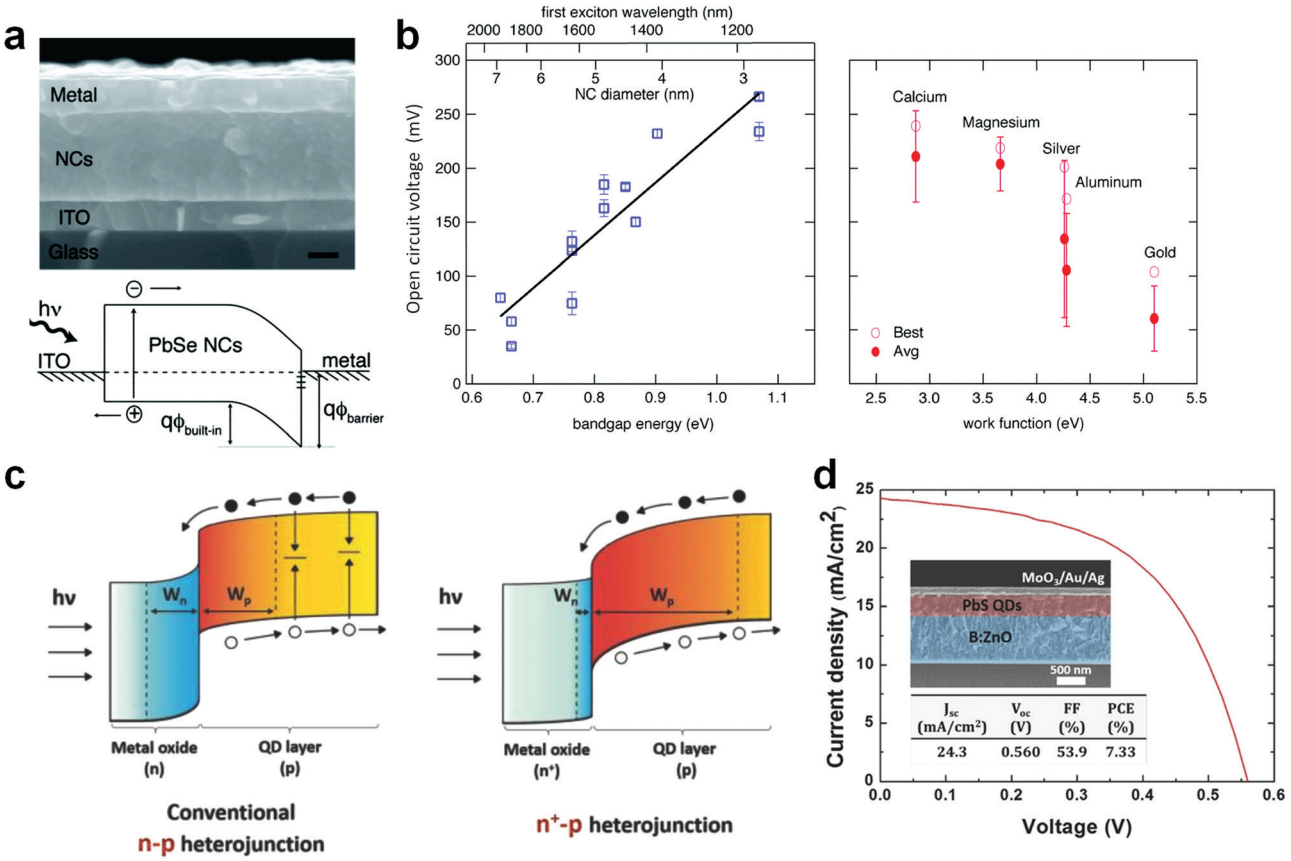

Fig. 4 Schottky and depleted heterojunction CQD-SCs. (a) Cross sectional scanning electron microscopy (SEM) and schematic diagram of Schottky CQD-SC. Scale bar represents 100 nm. (b) V_{OC} trends in Schottky CQD-SCs with different CQD sizes (different E_g) and work function of the metal electrode. Reproduced with permission from ref. 19. Copyright 2008, the American Chemical Society. (c) Schematic energy band diagram of conventional and n-doped ETL employed depleted heterojunction CQD-SCs. (d) J–V characteristic of depleted heterojunction CQD-SC with a boron-doped ZnO layer as a transparent electrode. The inset shows the cross sectional SEM image of the device and the photovoltaic performance table. Reproduced with permission from ref. 73. Copyright 2016, Wiley.

the ETL and CQD allows one of the main limitations of Schottky CQD-SCs to be overcome (Fig. 3(b)). Photogenerated charge carriers are created in the junction region and can be efficiently extracted by the ETLs. Furthermore, the ETLs block hole transport from the CQD layers to the cathode, thereby resulting in reduced non-radiative electron–hole recombination. Early studies on depleted heterojunctions focused on energy level alignment between the CQD layers and charge transport layers (CTLs) by controlling the CQD diameter or thickness.[20,74] A comparison between depleted heterojunction and Schottky-type SCs revealed that higher V_{OC} and FF values can be obtained by implementing proper CTLs.[75] E_g tuning of CQDs allows the formation of different junction kinetics at the interfaces, resulting in a PCE of 5.1%.[23] Most studies have focused on the modification of ETLs. ZnO nanoparticles have been used as ETLs and formed heterojunctions with 1.3 eV bandgap PbS QDs, resulting in a certified PCE of 2.94% with cells that are stable over 1000 h.[21] Mesoporous TiO_2 also elongates the depletion region between the ETL and the CQD layer, which improves charge extraction at the junction region. Thus, thicker CQD layers can be applied, which results in enhanced light absorption. As a result, the short circuit current density (J_{SC}) almost doubles, and a PCE of 5.5% can be achieved.[24] For better charge collection efficiency, mesoporous TiO_2 has been modified to a more periodic pillar structure. The charge carriers generated at the deeper region in the device were optically demonstrated to be efficiently extracted by periodic ETLs. This modification extended the depletion region two-fold and led to a hysteresis-free PCE of 5.7%.[29] Mesoporous-type CQD-SCs were further optimized with a TiO_2 nanonetwork structure, and a PCE of 7.3% was achieved.[32] In addition, UV-ozone treatment of ZnO allowed control of the depletion region. The corresponding thickness of the CQD layer was increased, which resulted in an enhanced PCE.[76] ZnO was also modified to nanowire structures to enlarge the surface area of the thick depletion region. The use of highly n-doped ZnO layers with boron doping increased the depletion region on the junction side (Fig. 4(c)). A PCE of 7.55% was reported for CQD-SCs employing n-doped ZnO, and even when the n-doped ZnO layer was used as a transparent electrode, a PCE of 7.33% was obtained (Fig. 4(d)).[73] Chemical modification of the ZnO surface reduced its surface trap sites. Photogenerated charge carriers in the depletion region were efficiently extracted by a 1,2-ethanedithiol (EDT) ligand-treated ZnO layer, resulting in a

certified PCE of 10.14%.[43] Additionally, metal oxide and p-type polymer layers are widely adopted as a hole transporting layer (HTL) in CQD-SCs. The optimization of CQD layers by introducing a MoO_3 layer at the hole contact electrode resulted in a PCE of 4.3%.[77] Recently, PBDTTT-E-T, a copolymer of benzo[1,2-*b*:4,5-*b*′]dithiophene (BDT) and thieno[3,4-*b*]thiophene (TT), was introduced as an HTL in infrared (IR) CQD-SCs.[78] In addition, the introduction of a nanostructured HTL into the device, using nanoimprint lithography, enhanced light absorption at IR wavelengths. As a result, a record PCE (19.1 mW cm^{-2}, cut-off <1100 nm) of 6.83% was obtained under IR light (19.1 mW cm^{-2}, cut-off <1100 nm), which is suitable for tandem structures with commercialized c-Si SCs (absorbing light up to 1100 nm).

2.1.3 Quantum junction CQD-SCs. A heterojunction between inorganic CQDs was introduced into CQD-SCs in 2012 by Rath *et al.*[79] The purpose of a quantum junction is to extend the depletion region in the junction area. Photogenerated charge carriers can be efficiently separated in the junction region of the active layer. n-Type Bi_2S_3 CQDs and p-type PbS CQDs were used as a heterojunction. The advantage of using the heterojunction layer was an improved carrier lifetime, which minimizes recombination losses. The thickness and mixing ratio optimization of the QD junction resulted in a PCE of 4.87%. The E_g values of the PbS CQDs were controlled (0.6–1.6 eV) to align the energy levels of different quantum junctions. E_g matching between n- and p-type CQDs resulted in a certified PCE of 5.4%.[31] Furthermore, a comparison of the simulated efficiency trends between depleted heterojunction and quantum junction CQD-SCs demonstrated that the quantum junction has great potential to achieve a higher PCE by managing the E_g values of the quantum junctions. The initial stage of quantum junction SC research used Schottky-type cell structures. The order of the quantum junction (np- or pn-wise stacking) and corresponding metal electrode could be controlled to activate SCs under a forward or reverse bias current.[80] Quantum junction cells were further improved by applying additional charge extraction layers. TiO_2- and aluminium-doped ZnO (AZO) ETLs were introduced into PbS quantum junctions. A PCE of 6.1% was achieved by adding MoO_3 at the hole contact.[37] Furthermore, halide exchange has been intensively studied to utilize different doped CQDs, as shown in Fig. 5(a). Highly n-doped iodide-modified PbS CQDs, n-doped bromide-modified PbS CQDs, and p-doped mercaptopropionic acid (MPA)-modified PbS CQDs were applied to form a ternary junction, which extended the depletion region to approximately 330 nm (Fig. 5(b)). As a result, a PCE of 8.0% was reported.[38] The size of CdSe CQDs were tuned to realize proper band alignment between a ZnO ETL and PbS CQDs. The photogenerated charge carriers from the PbS CQDs as well as from the CdSe CQDs contributed to an improved J_{SC} value, thereby leading to a PCE of 7.5%.[81] n- and p-type CQDs were synthesized *via* a pre-ligand exchange method. The n–p quantum junction arising from pre-synthesized CQDs on top of a ZnO ETL showed a PCE of 10.94%, without the need for a complicated washing process.[55]

2.1.4 Band alignment. The structural development of CQD-SCs has been moving towards enlarging the depletion region and reducing the energy barrier at the junction between CQDs and CTLs for efficient charge extraction, as shown in Fig. 3(c). The band alignment structure of CQD-SCs aims to enhance these parameters *via* the introduction of additional CTLs and ligand exchange of the CQDs. For p-doped CQDs, the surface of the CQDs was treated using a short cross-linking ligand, 3-mercaptopropionic acid (MPA) or 3-mercaptobutyric acid (3-MBA). The p-doped CQDs with 3-MBA exhibited a larger depletion region, and the p^+-doped CQDs with MPA exhibited a larger quasi-Fermi level splitting, leading to a higher V_{OC} value. The combination of both ligands resulted in gradient

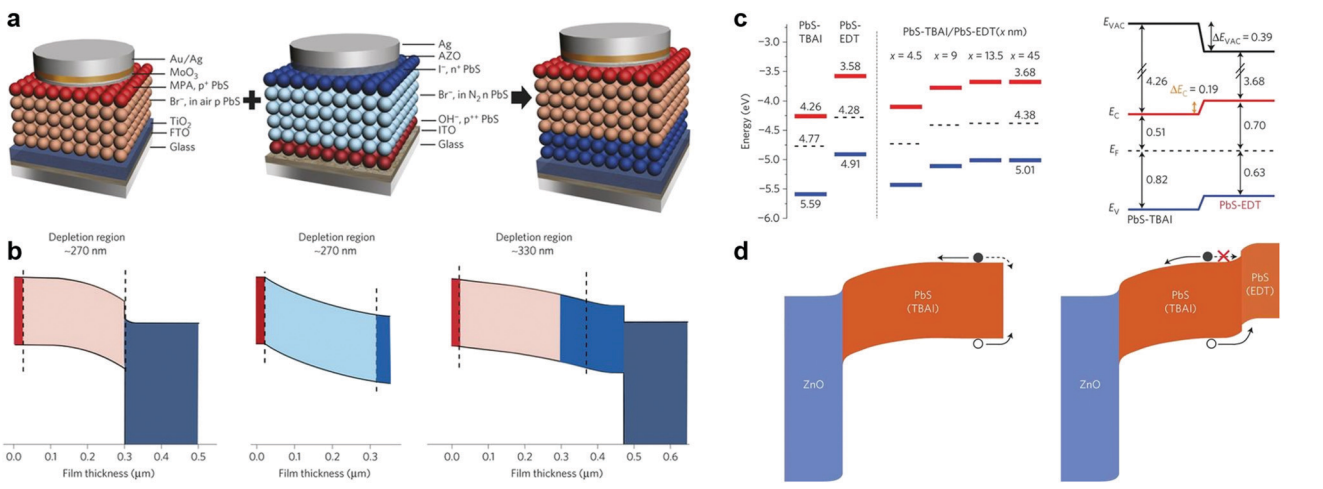

Fig. 5 Quantum junction and band alignment CQD-SCs. (a) Schematic of a ternary quantum junction constructed by combining conventional ($p–p^+$ junction) and inverted ($p^{++}–n–n^+$) quantum junction structures. (b) Corresponding simulated energy band diagram with depletion regions. Reproduced with permission from ref. 38. Copyright 2014, Springer Nature. (c) Energy levels of pure PbS-TBAI, PbS-EDT and PbS-TBAI with different thicknesses of PbS-EDT layers. The red and blue lines represent the conduction and valence band edges of the CQDs. The dashed lines represent the Fermi levels of the CQDs. (d) Proposed energy band bending under short-circuit conditions. Reproduced permission from ref. 35. Copyright 2014, Springer Nature.

band alignment with a PCE of 7.2%.[82] Tetrabutylammonium iodide (TBAI) and EDT were applied to CQDs as n- and p-type ligands, respectively. EDT-PbS CQDs showed band alignment with TBAI-PbS CQDs and even took on the role of electron blocking in the hole contact region (Fig. 5(c) and (d)). A certified PCE of 8.55% was recorded.[35] To estimate the underlying mechanism of carrier transport in TBAI- and EDT-capped CQDs, temperature-dependent electrical characterization of CQDs was conducted. Based on carrier lifetime, electron and hole diffusion length, doping concentration, and depletion width measurements, a highly p-doped CQD was required for V_{OC} value improvement. Moreover, the concentration of the p-type dopant should be one order of magnitude higher than that of the n-type dopant for efficient band alignment.[12] Ligands were further exchanged with methylammonium lead iodide ($MAPbI_3$) and thioglycerol (TG). Both $MAPbI_3$ and TG ligand exchange led to n-type properties. When n-type CQDs were mixed together, the charge transfer between the valence bands (VBs) of the mixed n-type CQDs was efficient compared to that in single CQD films. Thus, in donor–acceptor structure CQDs, an appropriate donor–acceptor ratio leads to balanced electron–hole pairs. As a result, a hysteresis-free PCE of 10.45% was reported.[52] Moreover, E_g control of IR-absorbable CQD ink, dissolved in a highly stable non-polar solvent, led to the formation of a graded back junction and an extended depletion region. A mixture of 1.4 and 1.3 eV n-type CQDs further absorbed light in the IR region, resulting in a PCE of 12.3%.[59] However, the introduction of a junction between HTL and CQDs has been less studied compared to ETL junctions because realizing smooth band alignment at the interface is difficult, and serious recombination frequently occurs at the interface. Furthermore, CTLs beneath the CQD layers need to be robust enough to endure chemical processes such as ligand exchange and CQD surface treatments. The high level of requirements for CTLs limits the materials that can be used. Wang *et al.* inserted a thin NiO film at the interface of an HTL and EDT-PbS or I^--PbS for gradient band alignment, achieving a PCE of 9.7%.[83] Based on n-type I^--PbS and p-type MPA-PbS CQD-SCs, a hole selective layer (HSL) was introduced on the hole contact side. The HSL prevented electron–hole recombination at the anode and efficiently extracted photogenerated holes, resulting in a PCE of 0.23%. Furthermore, a thick HSL layer works as an optical spacer, which enables more light to be absorbed in the active layer. Owing to optical management, CQDs with a V-compound parabolic trapper (enhancing light absorption) exhibited a PCE of 11.71%, arising from the improved J_{SC} value.[57] The exchanging of different ligands provides an efficient band alignment structure to realize larger depletion regions and less recombination losses in mixed CQD films. By introducing additional charge selective layers, both the PCE and lifetime of the device could be further improved.

2.1.5 Tandem structure. The layer thickness of CQDs is limited owing to the trade-off between charge extraction and light absorption. The physical parameters of CQDs, such as the charge diffusion length and depletion region, govern the optimal thickness of CQD layers. Hence, advanced structures for utilizing unabsorbed photons due to thin CQD layers are needed. One well-known strategy to convert more photons to electricity is a tandem structure consisting of stacked light-absorbing layers. The most important design factors of tandem cells are E_g tuning between each light-absorbing layer and design of a charge recombination layer between each sub-cell. Prototypes of tandem CQD-SCs, employing 1.0 and 1.6 eV nanocrystals, were reported by Choi *et al.*[84] The charge recombination layer included ZnO, thin Au (1 nm) and poly(3,4-ethylenedioxythiophene) polystyrene sulfonate (PEDOT:PSS). For efficient energy harvesting, metal oxide layers, such as MoO_3, ITO, AZO, and TiO_2, were adopted in tandem structures as charge recombination layers. The efficient electron–hole recombination at the inter-layer resulted in a PCE of 4.21%.[85] However, difficulties in tuning the E_g of CQDs led to the introduction of other types of light-absorbing layers, such as organic layers, to tandem devices. An organic heterojunction light absorber (poly(3-hexylthiophene), P3HT) and [6,6]-phenyl-C61-butyric acid methyl ester (PCBM) were used as the active layer of sub-cells in CQD tandem SCs. An inter-recombination layer with thin Al (1 nm) and WO_3 (15 nm) was used.[86] Further improvement of CQD tandem structures with organic absorbers was achieved by incorporating the low E_g polymer thieno[3,4-*b*]-thiophene/benzodithiophene (PTB7). Optimization of the inter-layers resulted in a PCE of 9.4%.[87,88] Tandem devices with perovskite SCs were achieved by introducing SnO_2 and PEDOT:PSS as a recombination layer. The E_g tuning of a PbS cell led the tuning of the V_{OC} value, which resulted in PCE of 11.03%.[89] For all-inorganic devices, inorganic CdTe nanocrystals have also been included in CQD tandem cells. E_g optimization of both PbS and CdTe CQDs with ZnTe and ZnO inter-recombination layers was conducted.[90] EDT-PbS CQDs, Au, PEDOT:PSS and ZnO nanocrystals were used as the charge recombination inter-layer. A downshift in the vacuum energy level arising from the inter-recombination layer allowed the use of the same light-absorbing layer for both sub-cells, achieving a PCE of 8.3%.[91] Chemical vapour-deposited graphene and AZO were introduced to the inter-recombination layer, forming efficient PbS CQD-based all-inorganic tandem SCs with a PCE of 8.2%, as shown in Fig. 6(a)–(d).[92] Recently, all-PbS CQD-based tandem SCs were achieved by introducing graded band alignment. The size of the CQDs was precisely controlled and the carrier transport in the charge recombination layer was enhanced, leading to a PCE of 6.8%.[93]

As we have discussed, the structural development trends of CQD-SCs are extending the depletion region and minimizing the recombination loss of photogenerated charges. An improvement in the materials could enhance the physical characteristics of CQDs, such as the charge diffusion length. However, there is more room for improvement in PV efficiencies through structural enhancements. Kim *et al.* suggested a close-packed CQD layer by pressing the film with an external force.[94] Introduction of an ordered structure to CQDs could be a method to overcome the losses in PV parameters. Recently, CQDs were structurally confined with a two-dimensional matrix using lead iodine (PbI_2) and amines (Fig. 6(e) and (f)).[62,95] A low dimensional

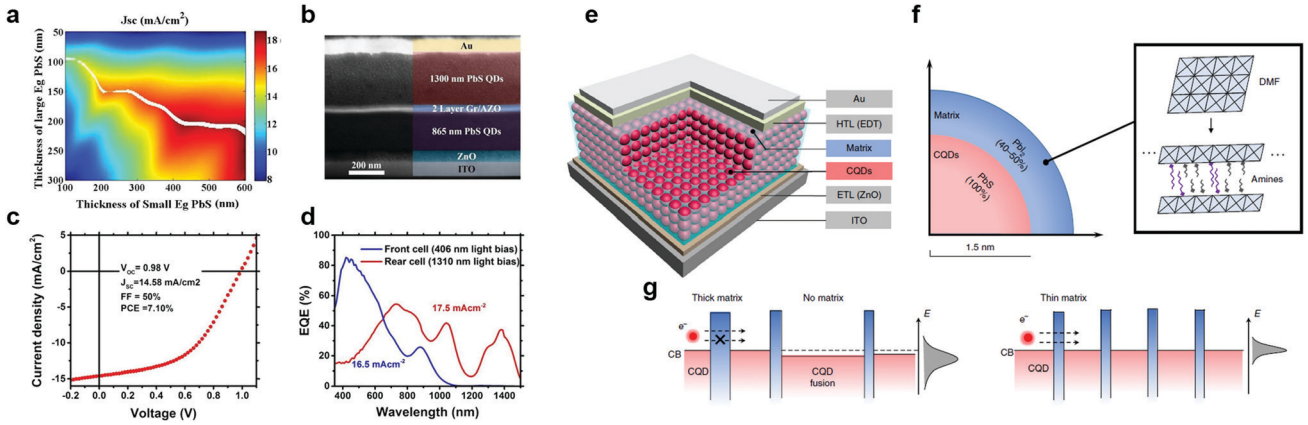

Fig. 6 Tandem and 2D structured CQD-SCs. (a) Simulated achievable J_{SC} values in the tandem devices based on the active layer thicknesses. The white line suggests the optimum thicknesses of each CQD layers. (b) Cross sectional SEM of a tandem CQD-SC. (c) J–V characteristics of the tandem CQD-SC. (d) EQE of each of the sub cells of the tandem device. Reproduced with permission from ref. 92. Copyright 2018, the American Chemical Society. (e) Schematic diagram of the 2D matrix architecture, where CQDs (red) are assembled in a matrix medium (blue). (f) The matrix component is PbI_2. The molecular ratio is about 40–50% compared to PbS, which is a sufficient enough amount to cover a full monolayer. (g) Homogeneity of the matrix reduces structural and energetic disorder. The diffusion length and V_{OC} value increase with the homogeneity. Reproduced with permission from ref. 62. Copyright 2018, Springer Nature.

device structure induces structural ordering of the CQDs, which significantly reduces their energetic disorder, as shown in Fig. 6(g). A possible advantage of ordered CQDs is the extension of their intrinsic diffusion, showing efficient charge extraction even for thick CQD layers. The reported high PCE of 12.48% implies that the research direction of the structural development of CQD-SCs is promising. Perovskite-based CQD-SCs have emerged with phase stability and a desirable bandgap. The presence of cubic phase $CsPbI_3$ CQD-SCs boosted the development of perovskite-based CQD-SCs.[47] CQD surface treatment with methyl acetate allowed a compact and electrically conductive film state, resulting in a PCE of 10.77% (Fig. 7(a)–(c)). The bandgap tuning of nanocrystals was easily achieved by substituting in halide ions, making the application of perovskite-based CQDs more feasible for use in optoelectronic devices.[96] Further improvements in $CsPbI_3$ SCs were reported by cooperating organic perovskite species (formamidinium) or inorganic salts to Cs cation. The larger absorbance range and improved electrical coupling in the active layer improved the photovoltaic performances.[54,66,97,98]

2.2 Device structure engineering

Understanding the role of each constituent layer of CQD-SCs is essential in optimizing the device efficiency and stability. The charge transport characteristics between each interface play important roles in the device performance. This section covers the device physics for each device constituent layer: CQDs, CTLs and electrical contacts.

2.2.1 Ligand exchange and CQD passivation. Highly concentrated, stable CQD films are essential for the commercialization of CQD-SCs. For the stable dispersion of CQDs in organic solvents, long chain ligands, such as oleic acid, have been widely used.[35] These long chain ligands exhibit insulating properties that hinder dot-to-dot carrier transport. If CQDs with long chain ligands are used for the light-absorbing layer in PV devices, the collection efficiency of photogenerated charges is low. Furthermore, the long chain ligands and surface defects of CQDs function as the non-radiative recombination centres of photogenerated charge carriers, decreasing the V_{OC} and FF values of the SCs. Hence, to achieve efficient carrier

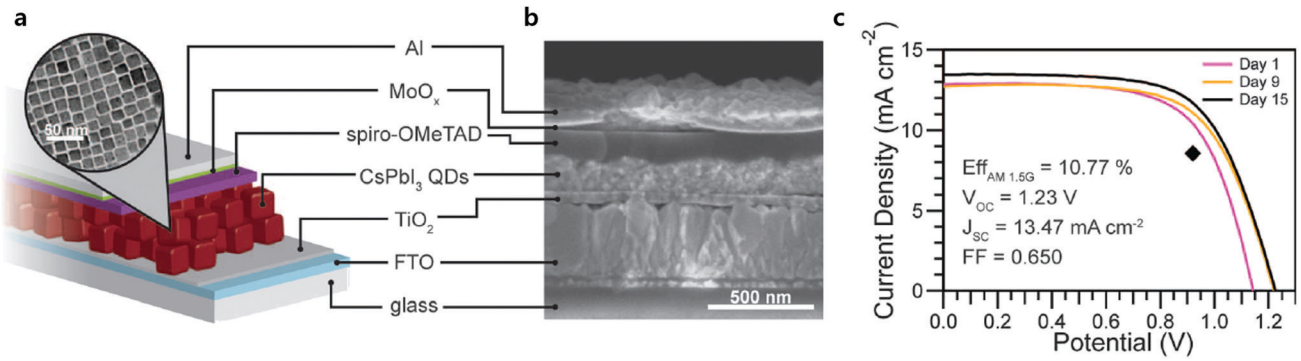

Fig. 7 Perovskite-based CQD-SCs. (a) Device structure of $CsPbI_3$ CQD-SCs. (b) Corresponding cross-sectional SEM image. (c) Photovoltaic performance in terms of device storage time. The black diamond represents the stabilized power output at 0.92 V. Copyright 2016, AAAS.

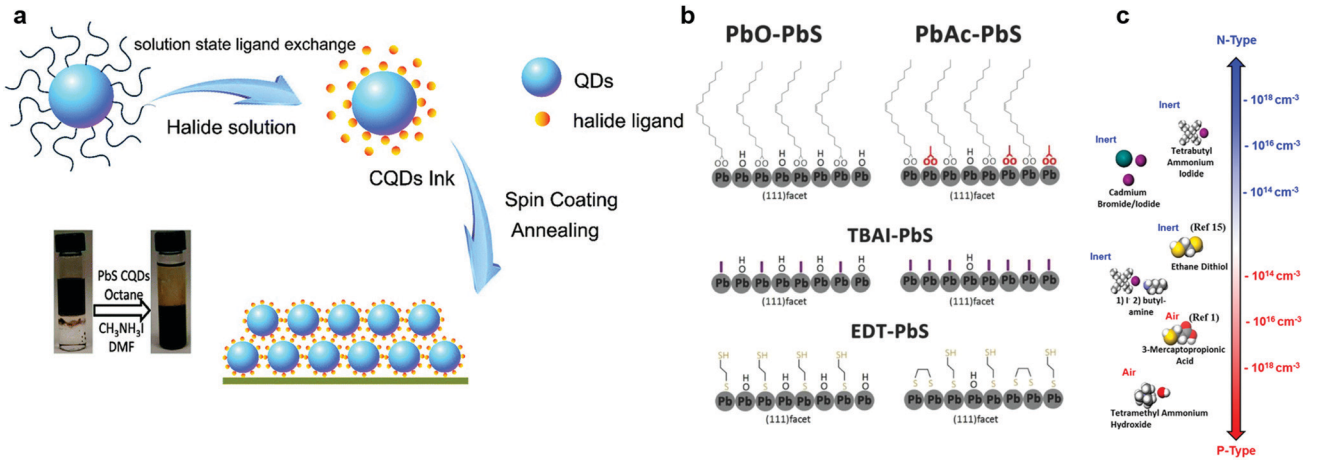

Fig. 8 (a) Schematic diagram of solution phase ligand exchange with a halide solution. Long insulating OA chains are efficiently exchanged to short halide ligands. Reproduced with permission from ref. 99. Copyright 2016, the Royal Society of Chemistry. (b) Schematic images of the (111) facet of CQDs from PbO and $PbAc_2{\cdot}3H_2O$ before and after the ligand exchange process, where acetate ligands replace the hydroxyl groups during the CQD synthesis. In the final solution, after ligand exchange, the number of hydroxyl groups was significantly reduced using acetate ligands. Reproduced with permission from ref. 61. Copyright 2018, Wiley. (c) Doping density variation according to the effect of ligand exchange under air or inert conditions. Reproduced with permission from ref. 100. Copyright 2012, the American Chemical Society.

transfer inside CQD films, improvement of the film conductivity of the CQD layers is required, which can be achieved by exchanging long chain ligands with short ones, as shown in Fig. 8(a). Ligand exchange shortens the distances between the CQDs and increases their packing density, thereby resulting in more efficient charge transport in the CQD film. Also, n- or p-type CQDs with carrier density variation can even be achieved by doping, as shown in Fig. 8(c). An atomic ligand with halide ions (I^-, Cl^-, Br^-) can passivate a the defect states of a CQD and control its energy levels.[27] Ip *et al.* reported that the mid-gap states of a CQD act as additional electron trap sites for photo-generated electron–hole pairs.[28] Thus, mid-gap trap states are one factor that restricts the PV performance of CQD-SCs. Since the passivation of defect states at CQD surfaces is normally performed in solution rather than in solid films, halide anions are used as passivating materials for the defects. As a result of surface passivation by halide ions, the binding strength between CQDs and ligands is improved, and defects within the bandgap can be successfully suppressed. Halide ligand exchange also protects CQDs from oxygen penetration, allowing successful synthesis of air-stable n-type CQDs.[38] Additionally, organic short ligands, such as MPA, EDT, and TBAI, have been suggested for improving the electrical characteristics of CQD films. Long insulating oleic acid ligands have been exchanged with EDT (p-type) and TBAI (n-type).[35] The successful band alignment of p- and n-type CQDs employing EDT and TBAI led to efficient carrier transport in the device. Further studies were performed to passivate defect states on the CQD surfaces. Liu *et al.* reported that organic–inorganic hybrid ligand exchange sharpened the band tails and decreased energy funnelling.[101] The native hydroxyl ligand in CQDs affects the PV performance, so this ligand should be removed or replaced.[44] The passivation of hydroxyl defect states by a hybrid ligand has been shown to improve the device efficiency and stability. The deep density of traps on the Pb surface have been passivated *via* I^- doping with a 1.5% I/Pb ratio during the PbS synthesis process.[51] Ligand exchange of pseudohalides, such as the thiocyanate anion (SCN^-), was reported to passivate the deep trap states at the CQD surfaces.[102] The hydroxyl ligands were partially replaced by introducing lead acetate trihydrate (PbAc) during CQD synthesis. The acetate formed efficient capping ligands with oleic acid, replacing the hydroxyl ligand and enhancing the device performance, as shown in Fig. 8(b).[61] Recently, sodium acetate was shown to prevent CQDs from aggregating and passivate the facet defect states of CQDs.[103] Recent approaches such as UV treatment and oxygen-plasma treatment on CQD surfaces have allowed the reduction of the density of hydroxyl groups at CQD surfaces, inducing effective p-doping on CQDs.[104,105]

2.2.2 CTLs. The improvement in materials engineering led to the development of different energy band CQDs. The n- or p-type tunability of CQDs *via* ligand exchange or surface passivation initiated structural development focused on CTLs. The efficient collection of photogenerated charge carriers requires three properties: (1) step-wise band alignment between CQDs and CTLs, (2) proper electron–hole mobility balance, and (3) photophysical stability of each layer.

The variation in the optimum conduction band (CB) and VB of CTLs depends on the size of the CQDs, implying that an optimum QD size exists for proper CTLs. As the E_g of a CQD varies depending on its size, CTLs should be carefully chosen considering the energy level of the CQD and its VB and CB. Furthermore, simulation results indicate that the thickness of the CTL plays an important role in balanced charge extraction and electric field redistribution, which is closely related to the maximum J_{SC} values in CQD devices.[106] In particular, the injection dynamics of photogenerated charges from CQD layers to ETLs could be limited by the photoconductivity of the ETLs.[107] To realize efficient charge extraction to an ETL, the

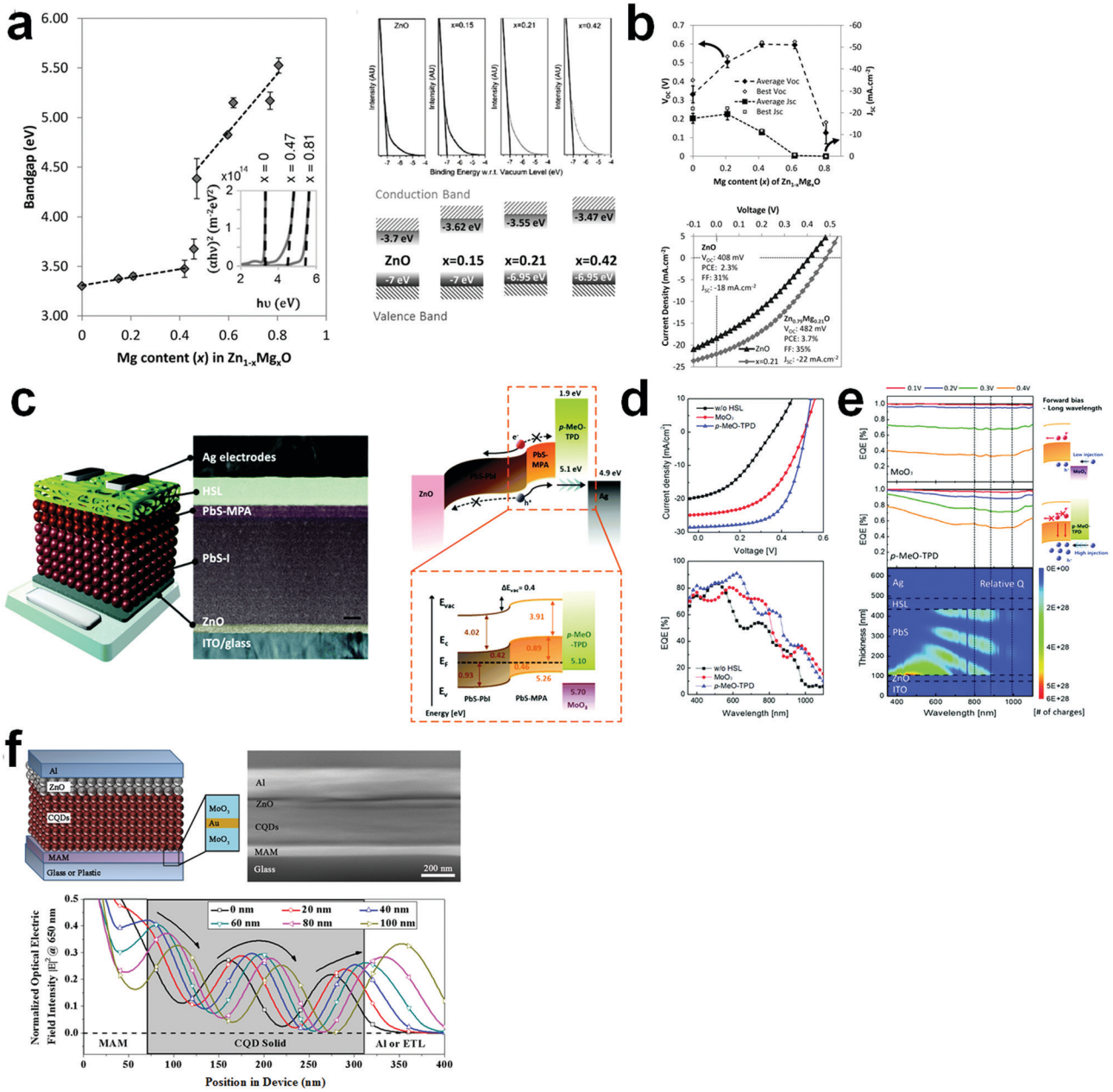

Fig. 9 Device engineering of charge transport layers and metal electrodes. (a) The E_g of ETL (ZnO) tuned *via* the magnesium doping ratio. The valence band of both doped and undoped ZnO layers exhibits no changes. The conduction band edges of doped ZnO are calculated using the UPS data and E_g measurements. (b) The device performances with J_{SC} and V_{OC} variation regarding the magnesium doping effect on ZnO. Reproduced with permission from ref. 109. Copyright 2014, Wiley. (c) Schematic of a CQD-SC integrating an organic hole selective layer, or HTL. The corresponding energy level alignment of each of the layers under short circuit conditions is depicted. (d) *J*–*V* characteristics and EQE values of the devices with/without a HTL. (e) Normalized forward biased EQE of CQD-SCs and the charge generation profiles of the device structures. Reproduced with permission from ref. 57. Copyright 2018, the Royal Society of Chemistry. (f) Schematic of the DMD structured CQD-SC and normalized optical electric field intensity within the device at an incident wavelength of 650 nm. Reproduced with permission from ref. 119. Copyright 2016, Elsevier.

photoconductivity of ETLs (mainly TiO_2 or ZnO) and their doping process have been widely investigated. Zr or Sb was doped with TiO_2 to achieve higher mobility (0.015 to 0.026 $cm^2 V^{-1} s^{-1}$). Together with CB tuning of the doped TiO_2, the PV performance was improved.[26] The accumulated carrier density inside the PbS CQD layer was effectively decreased by introducing n-doped PCBM on top of TiO_2.[108] In particular, elemental doping of ZnO led to improved conductivity and better PV performance of the device. Mg doping was performed to induce a band shift in ZnO (Fig. 9(a) and (b)).[109,110] In addition, In atoms contribute to enhanced light absorption of ZnO-incorporated CQD-SCs by filling the vacancy states of the ZnO film and decreasing its parasitic absorption. The CB energy level was tuned by adjusting the In doping concentration to maximize photogenerated

charge carrier extraction.[111] Moreover, Cl, Cs, or K were also introduced to dope ZnO, tuning its E_g and energy level.[49,56,112] Additionally, surface passivation of ZnO boosts the performance of ZnO-containing CQD-SCs. The ZnO surface was passivated using WPF-6oxy-F to enhance the V_{OC} value. The introduction of a surface dipole to the ZnO surface induced a larger Fermi level splitting at the junction.[42] The junction properties between the CQDs and ZnO were improved by introducing a poly(vinylidenefluoride-trifluoroethylene) (P(VDF-TrFE)) layer. The porous P(VDF-TrFE) exhibits piezoelectric characteristics that generate a converging electric field at the junction.[113] The introduction of a three-dimensional graphene network at the ETL/CQD junction interfaces reduced fast electron recombination, which enhances charge collection to the electrode.[114] Moreover, the introduction of nanostructured ETLs boosts photovoltaic performance by enhancing charge extraction at the CQD-ETL junctions. The increased interfacial area reduces the trap-related recombination and enhances bimolecular recombination. The ordered nanopillar structures of TiO_2 enhance absorbance to the photoactive layer, suppressing trap-related recombination.[29] The porous TiO_2 template enhances increased light absorption with charge de-trapping.[115] Vertical arrays of ZnO nanowires decouple light absorption from carrier collection at the junction interface, enhancing the photovoltaic performance by 35%.[77] Recently, high-performance CQD-SCs were achieved by combining optical management strategies such as ZnO nanowires and energy down-shifting CQD optical conversion layers.[116]

In early studies, the structural development of CQD-SCs was focused on forming efficient junctions between CQDs and ETLs, because PbS-based CQDs generally exhibit p-type characteristics enabling hole transport through them. Most reports on HTLs have focused on minimizing the energy barrier between CQDs and electrodes and introducing materials that have high hole conductivity for efficient extraction of photogenerated holes. For band alignment between CQDs and HTLs, CuI was introduced to enable step-wise hole extraction to the electrode.[117] Graphdiyne was inserted between an Au electrode and a CQD layer to reduce charge recombination at the electrode-HTL interface.[45] An organic HTL was applied to passivate a CQD surface. *N*,*N*,*N*′,*N*′-Tetrakis(4-methoxyphenyl)-benzidine (*p*-MeO-TPD) efficiently was shown to extract photogenerated holes and block drifting electrons, thus decreasing electron–hole recombination at the metal electrode, as shown in Fig. 9(c)–(e). Moreover, regarding the device stability in ambient air, an HTL layer has been shown to protect CQDs from oxygen penetration.[57] A study on the effect of the hole mobility of a HTL revealed that the hole mobility has significant importance, along with the proper energy level alignment with CQDs, indicating that a PCE of over 15% could be reached if the high hole mobility ($\sim$0.1 cm^2 V^{-1} s^{-1}) and deep HOMO level ($\sim$5.4 eV) PTB7 layer could be tuned.[118]

2.2.3 Electrical contacts. The foremost property of electrodes in SCs is the matching of the work function to the energy levels of the CTL or CQD layers. As proven for many optoelectronic devices, the formation of an ohmic contact at the electrode is very important.[120,121] The work function of FTO was tuned to facilitate electron extraction.[33] Shallow work function FTO was operated with relatively thin ETLs (10 nm) and the depletion region was extended by 10%, showing improved PV performance. Work function control of metal counter electrodes has also been widely studied. p-Type CQDs require proper band alignment with the work function of metal electrodes and Au electrodes exhibit a higher work function than Al (4.3 eV) and Ag (4.7 eV) electrodes.[25] Au reduces the energy barrier with the HTL compared to Al or Ag, which results in a lower series resistance of the CQD-SC. Further improvement in the shunt resistance of the devices has been achieved by introducing a thin layer of MoO_3.[25,122] The energy level of the MoO_3 layer was pinned to the VB of CQDs, which lowered the energy level barrier between the CQDs and metal electrodes. Non-radiative recombination at the anode/MoO_3 interface was inhibited, resulting in higher J_{SC} and V_{OC} values, with higher shunt resistance in the device. When noble Au was replaced with Ni because of its cost savings and proper work function alignment with the VB of CQDs,[22] sulfur interdiffusion from the CQDs to Ni electrodes deteriorated the PV performance. The introduction of thin LiF efficiently blocked sulfur inter-diffusion, and the photogenerated charges were extracted to the Ni electrode through a thin tunnelling barrier.

Based on their efficient charge extraction properties, metal electrodes and transparent electrodes can be modified to manage light confinement in light-absorbing layers. Nanostructured diffraction gratings at an ITO surface allow increased re-absorption of light reflected from counter metal electrodes. Additionally, the amount of incoming light through the nanostructured ITO is increased.[123] Zhang *et al.* introduced dielectric–metal–dielectric (DMD) structures to the transparent anode, as shown in Fig. 9(f).[119] In the DMD structure, a thin metal layer is sandwiched between each dielectric, such as MoO_3. The DMD structure maximizes the optical transparency by utilizing refractive index matching between the metal and dielectrics. Through optical management, absorption by the anode and re-absorption of the light reflected from the counter metal electrode by the CQDs were maximized. Furthermore, an optical spacer was installed to re-distribute the electric field in the active layer, which provides maximized light absorption at the CQD layers. Additionally, the counter metal electrode could be replaced by DMD structures to realize all-transparent electrodes for CQD-SCs.[124] Recently, semi-transparent CQD-SCs were fabricated using a graphene electrode, which shows around 60% transmittance at 550 nm.[125]

2.3 Carrier multiplication

The Shockley–Queisser limit of the efficiency of single junction PVs is based on the assumption that an absorbed photon at the most generates one electron and hole pair.[126] A hot electron excited by high energy (more than two-fold E_g) in a QD has the potential to generate additional electron–hole pairs when it relaxes from a higher energy state to the $1S_e$ energy state. The high energy state of hot electrons could be lost *via* heat, but in some cases, this high energy state additionally excites electrons from the ground state, forming additional electron–hole pairs.

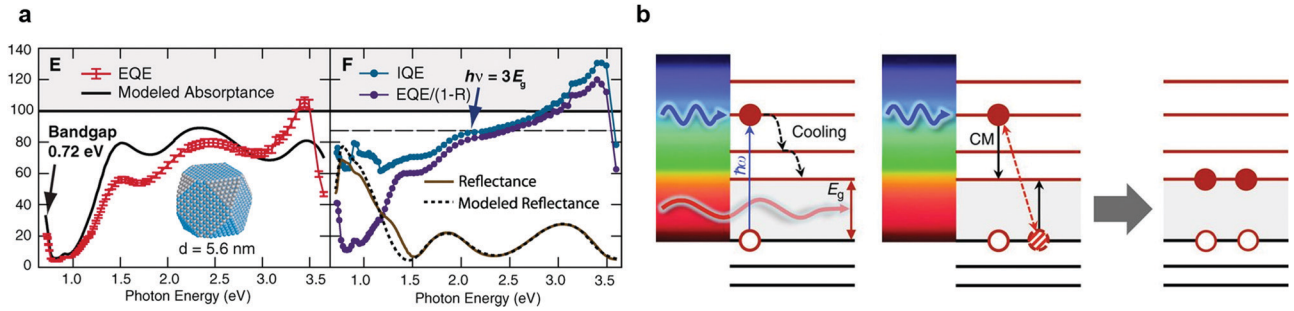

Fig. 10 Carrier multiplication. (a) The measured EQE and IQE values of over 100% in CQD-SCs. IQE begins to rise at a photon energy larger than $3E_g$. Reproduced with permission from ref. 14. Copyright 2011, AAAS. (b) Schematic of energy losses in a device from cooling of hot carriers and schematic of the CM process. Reproduced with permission from ref. 141. Copyright 2014, Springer Nature.

The inverse Auger recombination process of hot electrons has been reported in the form of carrier multiplication (CM) or multiple exciton generation (MEG) (Fig. 10(b)).[127,128] In theory, SCs capable of MEG are expected to overcome the Shockley–Queisser limit. The effects of CM on bulk semiconductor materials and CQDs have been widely compared.[127–135] The materials that show quantum confinement effects, such as CQDs, may slow down hot electron relaxation,[136] and the extra energy from the excitonic transition can be utilized for energy harvesting. Size and structure tuning of CQDs have been widely studied because CM is controlled by the amount of incident photon energy compared to the E_g.[128,137,138] In 2009, the first optoelectronic devices that showed over 100% EQE and internal quantum efficiency (IQE) were reported.[139] The photoconductivity at an incident photon energy of over $2.7E_g$ exhibited significant enhancement. This reported CM threshold, $2.7E_g$, exceeded the theoretical calculation by Klimov *et al.*[137] In PbS or PbSe CQDs, the expected threshold for CM was reported as $3E_g$, because the effective masses for electrons and holes are similar. The first PVs that utilized CM were reported in 2011 by Semonin *et al.*[14] As shown in Fig. 10(a), the devices using the 0.72 eV E_g of the PbSe CQDs achieved an EQE over 114% and an IQE over 130% under $3E_g$ excitation energy. The CM could be further enhanced by modifying the CQD structures. PbSe CQD nanorods exhibit a stronger Coulomb matrix than dot structures, which results in a 122% EQE and a 150% IQE from 0.8 eV E_g CQD nanorods.[140] However, to date, a high power conversion efficiency in CQD-SCs utilizing CM has not been reported. The device structures of CQD-SCs achieved to date may not be ideal for utilizing CM. Moreover, the CM threshold is still high, which needs to be further improved by materials engineering to control the relaxation process of hot electrons.

3. Stability

As the cost of electricity from SCs is determined by their efficiency and lifetime, the levelised cost of electricity (LCOE) is normally calculated using the following equation:

$$\text{LCOE (\$ per kW h)} = \frac{\text{total cost of installation and operation (\$)}}{\text{total amount of energy generated by a system (kW h)}}$$

If a photovoltaic system exhibits premature aging, the total amount of energy generated from the system shrinks, thereby resulting in a higher LCOE. Then, the system loses its competitive edge in the market. For instance, the LCOE of a device approximately decreases by half if its lifetime doubles. Hence, the stability of SCs is a key factor for their commercialization. Unfortunately, the device lifetime, whether the maximum power point tracking lifetime or storage lifetime, is a still a bottleneck in the commercialization of CQD-SCs, in comparison with commercialized c-Si PV systems. For example, the commercial c-Si solar panels from market leading companies (Jinko Solar, JA Solar, First Solar, Hanwha Q-cell and most other solar panel manufacturers) have a 25 year warranty for T_{80} (80% of initial efficiency) under standard test conditions (1000 W m^{-2}, AM 1.5 G, 25 °C). They also guarantee that the initial drop of their product is less than 4% within 1 year.[142] Since the device stability has been the most limiting factor for the commercialization of CQD-SCs, it has been continuously investigated and enhanced. Table 2 shows the development of device stability with respect to device structure, measurement conditions and publication year. The stability of CQD-SCs exceeds 1100 h (T_{80}, under illumination) and has been increasing. The stability merit could be an intuitive tool for comparing the stabilities of CQD-SCs to those of commercialized c-Si SCs (Fig. 11). The stability merit represents the importance of the stability in addition to the PCEs of the devices. Although a large gap still exists between c-Si SCs (green dashed lines in Fig. 11) and CQD-SCs, much room remains in extending the device lifetime of CQD-SCs by improving the materials or device engineering. In this section, we will discuss the effects of the most common device degradation sources and the strategies for overcoming these device degradation processes.

3.1 Degradation mechanisms

3.1.1 Oxygen and humidity degradation. When Pb-based CQDs react with ambient air, lead sulfite ($PbSO_3^{2-}$) or sulfate ($PbSO_4^{2-}$) can form on their surfaces (Fig. 12(a) and (b)).[150,151] $PbSO_3^{2-}$ has been reported to create shallow trap states (depth ~0.1 eV), while $PbSO_4^{2-}$ generates mid-gap trap states

Table 2 Stability table of CQD-SCs

Device type	Device structure	Measurement conditions (dark)	Measurement conditions (illumination)	Device stability (dark)	Device stability (illumination)	PCE (%)	Stability merit (dark)	Stability merit (illumination)	Published year	Ref.
Schottky	ITO/PbS/LiF/Al/Ag	Ambient air storage	—	60% at 160 h	—	2	1.2	—	2010	71
Depleted heterojunction	ITO/ZnO/PbS/Au	—	0.7 sun illumination	—	90% at 1000 h	2.94	—	2.65	2010	21
Depleted heterojunction	ITO/PbS/PbS–Ag/AZO/Ag	—	MPP (encapsulated)	—	90% at 60 h	6.1	—	5.49	2012	30
Schottky	ITO/PbS/LiF/Al/Ag	Ambient air storage	—	55% at 500 h	—	3.39	1.86	—	2014	70
Schottky	FTO/PEI/PbS/MoO_3/Au–Ag	Ambient air storage	—	70% at 450 h	—	3.8	2.66	—	2014	72
Band alignment	ITO/ZnO/PbS–TBAI/PbS-EDT/MoO_3/Au	Ambient air storage	—	99% at 150 d	—	8.55	8.46	—	2014	35
Band alignment	FTO/TiO_2/PbSe–PbI_2/PbSe-MPA/Au	Ambient air storage	—	99% at 60 d	—	6.47	6.41	—	2015	143
Depleted heterojunction	FTO/ZnO/TiO_2/PbS/Au	Ambient air storage	—	99% at 130 d	—	6.13	6.07	—	2015	144
Depleted heterojunction	FTO/TiO_2/PbSe/Au	Ambient air storage	1 sun illumination	75% at 2000 h	70% at 3.5 h	3.5	2.63	2.45	2016	145
Band alignment	ITO/ZnO/PbS-I/PbS-EDT/Au	Nitrogen storage	1 sun illumination (nitrogen)	97% at 30 d	80% at 1100 h	9.6	9.31	7.68	2016	44
Band alignment	ITO/ZnO/PbS-TBAI/PbS-EDT/GD/Au	Ambient air storage	—	95% at 120 d	—	10.64	10.11	—	2016	45
Band alignment	FTO/TiO_2/$CsPbI_3$/spiro-OMeTAD/MoO_x/Al	Desiccator	—	100% at 64 d	—	10.77	10.77	—	2016	47
Band alignment	ITO/ZnO/PbS (PbX_2/AA)/PbS-EDT/Au	Ambient air storage	—	90% at 1000 h	—	11.28	10.15	—	2017	101
Band alignment	ITO/IZO/PbS-TBAI/PbS-EDT/Au/TeO_2	Ambient air storage	MPP	95% at 70 d	90% at 0.9 h	7.3	6.94	6.57	2017	146
Band alignment	ITO/ZnO-SAM/PbS-PDMII/PbS-PDT/Au	Ambient air storage	MPP	95% at 24 d	97% at 4.5 h	10.89	10.35	10.56	2017	48
Band alignment	ITO/MZO/PbS-TBAI/PbS-EDT/Au	Ambient air storage	MPP	90% at 103 d	95% at 1 h	10.4	9.36	9.88	2017	53
Quantum junction	ITO/ZnO/n-PbS/p-PbS/Au	Ambient air storage	—	80% at 100 d	—	10.94	8.75	—	2018	55
Band alignment	ITO/ZnO/PbS-I/PbS-MPA/HSL/Au	Ambient air storage	—	90% at 180 d	—	11.71	10.54	—	2018	57
Band alignment	ITO/ZnO-K/PbS-I/PbS-PDT/Au	Ambient air storage	1 sun illumination	95% at 90 d	95% at 10 h	10.8	10.26	10.26	2018	56
Band alignment	ITO/ZnO/PbS–PbI_2/PbS-EDT/Au	Ambient air storage	—	70% at 365 d	—	11	7.7	—	2018	2
Band alignment	ITO/MZO/PbS-PbX_2/PbS-EDT/Au/MgF_2	Ambient air storage	1 sun illumination (white LED)	99% at 103 d	85% at 540 h	8.4	8.32	7.14	2018	147
Band alignment	ITO/MZO/PbS-$CsPbI_3$/PbS-EDT/Au	Ambient air storage	MPP	99% at 43 d	88% at 46 h	10.5	10.4	9.24	2018	148
Band alignment	ITO/CsZnO/PbS-TBAI/PbS-EDT/Au	Ambient air storage	—	97% at 90 d	—	10.43	10.12	—	2018	112
Band alignment	ITO/ZnO/PbSe–PbI_2/PbS-EDT/Au	Ambient air storage	—	94% at 1000 h	—	10.68	10.04	—	2019	149
Band alignment	ITO/PTAA/$CsPbI_3$/C60/BCP/graphene	Ambient air storage (20% RH)	—	96% at 14 d	—	5.11	4.91	—	2019	125
Band alignment	ITO/ZnO/PbS-TBAI/PbS-EDT/Au	Ambient air storage (50% RH)	—	90% at 90 d	—	8.9	8.01	—	2019	105
Band alignment	ITO/ZnO/PbS-TBAI/PbS-EDT/Au	—	1 sun illumination (N_2)	—	96% at 230 h	10.6	—	10.18	2019	104

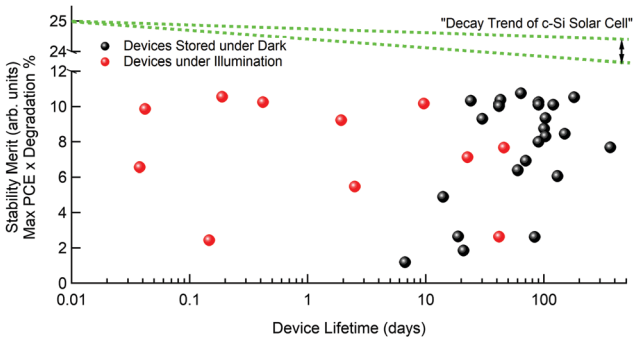

Fig. 11 Stability merits regarding the device lifetimes of CQD solar cells compared to a commercial c-Si solar cell. Stability merits are calculated by multiplying the maximum PCE and corresponding device degradation percentage. For example, the stability merit of a CQD-SC which exhibits a 10% maximum PCE and T_{80} (time that the PCE takes to decrease to 80% of the initial value) at 100 days can be calculated as 10 × 0.8 = 8. The green dashed lines represent the decay trend of a commercial c-Si solar cell. Here, it is assumed that the line represents a drop rate for the c-Si SC of around 2–4% (relative) in the first year of operation.[142] The black and red dots represent the stability merits of CQD-SCs in the dark and under illumination conditions, respectively. All the plotted data is based on that shown in Table 2.

(depth ~0.3 eV) around the CB of CQDs, which are critical for device performance and stability. Larger CQDs are prone to exposure to oxygen from air, exhibiting more $PbSO_4^{2-}$ than smaller CQDs after degradation. Moreover, volume shrinkage (~50%) of a CQD solution was reported when the solution was exposed to air. The 50% CQD solution was transformed to lead oxide components within 24 h. The effective core size of the CQDs decreased, enhancing the quantum confinement effect leading to a PL band shift.[152] The optoelectronic application of CQDs requires ligand exchange processes, as discussed in Section 2.2.1. During the ligand exchange process, the detached sites of long ligands can remain as empty sites without further short ligand attachment. Oxygen can become attached to such an empty site, acting as a defect state. This oxygen-induced quenching site provides additional trap states for photo-generated charge carriers, thus decreasing the PV performance and stability. In particular, both the non-polar (100) and polar (111) facets of Pb-based CQDs are easily exposed to oxygen and thus require passivation.[153] Kirmani *et al.* reported that the device performance is degraded when the devices are fabricated under high humidity or non-humidity-controlled conditions.[2] Down-shifting of the Fermi level of a p-type CQD *via* oxygen doping can enhance hole extraction, with reduced non-radiative recombination. However, a high humidity environment inhibits the effective oxygen doping of EDT ligand-based CQDs. Thus, the effective oxygen doping of p-type CQDs can be achieved by storing PV devices under dry air conditions. The degraded devices, fabricated under high humidity, can be recovered by storing them in a dry atmosphere. Once the device performance has recovered, the devices exhibit high stability under humid conditions.

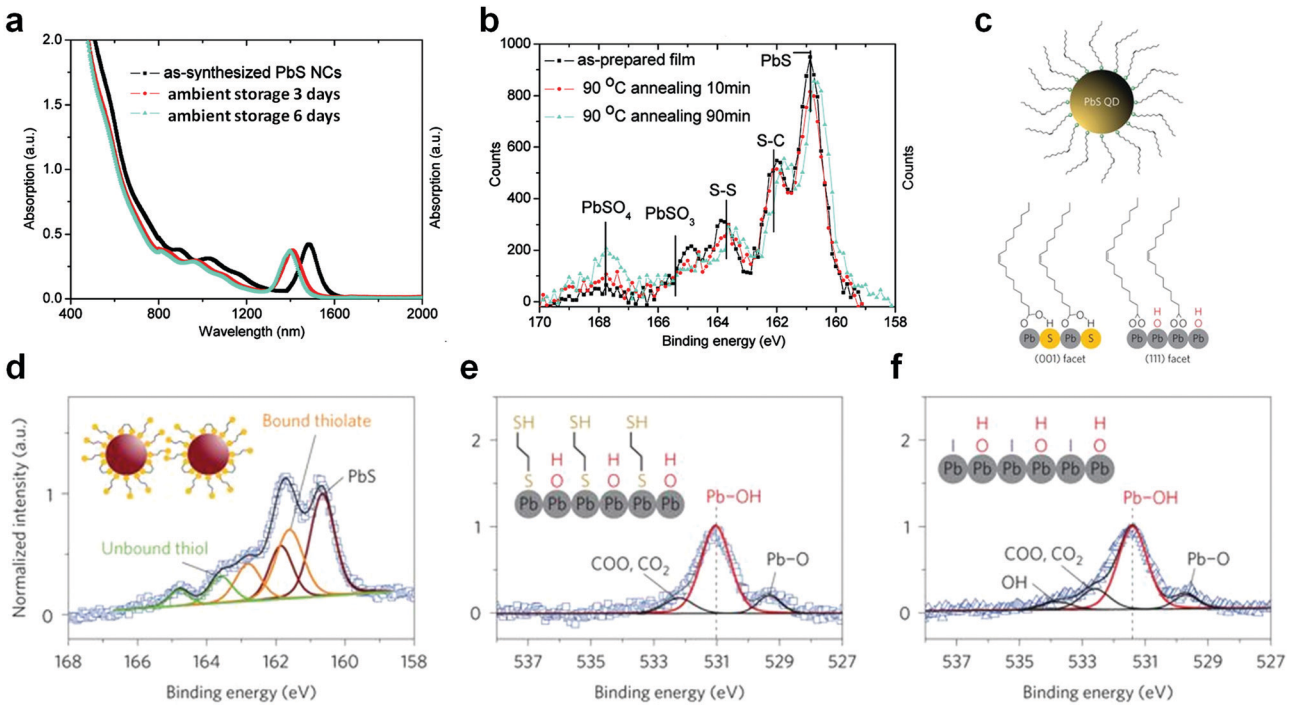

Fig. 12 Degradation sources of CQDs. (a and b) Comparison of oxidation characteristics measured using absorbance and X-ray photoelectron spectroscopy (XPS). The absorbance peak shifts according to CQD oxidation. The thermal degradation results increase lead sulfate formation. Reproduced with permission from ref. 150. Copyright 2010, the American Chemical Society. (c) Schematic figures of CQD with oleic surfactants showing that the (111) facet is occupied with hydroxyl groups. (d) XPS S 2p signals exhibit lead sulfite and sulfate formation on CQD surfaces. (e and f) XPS O 1s signals from EDT and TBAI ligand exchanged CQDs. The hydroxyl groups can still be detected after the ligand exchange process. Reproduced with permission from ref. 44. Copyright 2016, Springer Nature.

The dry-air-stored devices follow the same decay trend as PV devices fabricated under dry air conditions.

3.1.2 Light-induced degradation. The hydroxides on CQD surfaces have been reported to be unstable under light exposure.[154–156] The most widely used ligand exchange processes with EDT and TBAI were reported to lead to hydroxide species on Pb-terminated (111) surface facets, as shown in Fig. 12(c)–(f).[44] These hydroxide sites exhibit the quenching of photogenerated electrons and holes, thus increasing the non-radiative recombination rate, which is critical for device stability under illumination. Additionally, the most widely used ETL for record high-efficiency CQD-SCs is ZnO. Thus, investigation of the light stability of ZnO is worthwhile. Several reports on the photostability of intrinsic and modified ZnO have been presented,[48,56] and degradation of the ZnO interface or ZnO itself under illumination is expected. The sensitivity of ZnO or its light soaking behaviour under illumination has been reported for various types of SCs. Kim *et al.* reported that the ZnO layer is degraded under 1 sun illumination, causing increased energetic disorder around the CB edge.[157] Additional trap states were created, resulting in decreased V_{OC} values. Furthermore, oxygen-containing defects on the ZnO surfaces have been reported to cause inferior photostability.[158–160]

Some CQD-SCs exhibit interesting decay trends under illumination. The degraded PCEs recover to their original level or higher after storing the devices in the dark.[147,148] This self-healing process was also reported in perovskite SCs.[161] The light-activated meta-stable trap states can accumulate under light illumination. The charged region in the bulk leads to degradation of the photocurrent. When the devices are kept in the dark, these paths disappear, and the efficiency recovers. The degradation mechanism under light illumination should be considered as the combined effect of defect states on the CQD surfaces and in the interlayers of the device.

3.1.3 Thermal degradation. The formation of lead sulfite or sulfate at the CQD surface can be accelerated at elevated temperatures.[150] CQD films annealed at 90 °C for 10 min show increases in their oxygen composition from 6% to 9% depending on the CQD size. The XPS S 2p spectra of annealed CQDs imply that the amounts of both lead sulfite and sulfate can be increased by applying heat, as shown in Fig. 12(b). The increased lead sulfite and sulfate amounts induce additional trap states that lie below the CBs of the CQDs (0.1 and 0.3 eV for sulfite and sulfate), which cause degradation of charge extraction in SC applications. The thermal stability of ZnO, as investigated in the light degradation section, should contribute to the overall thermal device degradation. The thermal degradation effect in CQD devices was investigated in terms of the effect of AZO.[30] The device stability was very good for 3 h at 90 °C. The interfacial robustness arising from the AZO inhibited the formation of lead sulfate when the devices were heated. This result implies that a robust capping layer on the CQDs can effectively mitigate oxygen penetration, thus diminishing oxygen-induced thermal degradation. Thus, when the degradation study of CQD films is extended to devices, the effect of the thermal degradation of adjacent buffer layers should also be investigated. The inorganic parts in typical CQD-SCs, such as ZnO, TiO_2, and CQDs, can be considered to be stable at high temperatures. However, recent reports have introduced additional organic HTLs to realize efficient hole extraction, which can be considered unstable under high-temperature environments.[57,78,118] Thus, a more systematic investigation should be carried out on the thermal stability of advanced device structures with high PV performances.

3.2 Strategies to improve the device lifetime

Many studies on passivating degradation sources have been reported, as discussed in the previous section. To prevent dangling bonds created by oxygen penetration into CQDs, several strategies, such as ligand exchange or surface chemistry modification, have been developed. The packing density (higher stability) of CQDs was increased by a factor of two through a ligand exchange process with *n*-alkylthiolate compared to a *tert*-butylthiolate ligand exchange process.[162] Halide species (I^-, Br^-, Cl^-)-capped CQDs have been shown to be robust under oxygen exposure.[38,44,101,145,148] Overall, the iodide complexes showed better stability than bromides or chlorides, as shown in Fig. 13(a)–(e). The cation exchange from ZnSe using halides (PbX_2, X = I, Br, or Cl) allows CQDs to withstand oxygen and humidity.[143] In addition, shell structures were introduced to produce CQDs with core/shell structures and enhance the CQD stability.[163,164] The undesirable oxidation of PbS CQDs was inversely utilized to enhance CQD stability.[70] The amounts of lead sulfite and sulfate were increased by PbS oxidization, but the partial oxidization of PbS surfaces induced efficient Fermi level pinning between the electrode and CQDs, which raised the Schottky barrier and enhanced the light stability. A thin LiF layer was introduced between PbS and Al electrodes to prevent oxygen and moisture penetration. The delayed oxidization of both the PbS and Al electrodes made the device more stable.[71] The light-unstable hydroxide species could be replaced with photostable alkyl-terminated ligands, such as an oleic surfactant, which resulted in enhanced light stability.[165]

The most commonly used ETL, ZnO, has been modified to passivate unfavourable defect states on the surface. The thermal robustness of the entire device was enhanced by introducing aluminium dopants into ZnO.[30] Magnesium- and cesium-doped ZnO also exhibit enhanced robustness, with enhanced stability of the SCs,[53,112] potassium-doped ZnO shows enhanced light stability,[56] deposition of a thin layer of TiO_2 on a ZnO layer leads to enhanced stability,[144] and self-assembled monolayer (SAM) treatment of the ZnO layer makes the device more robust.[48]

Further stability enhancement was achieved by introducing an HTL passivation layer over the CQD layers. Single-walled carbon nanotubes were introduced as an additional hole extraction layer that significantly enhances the shelf-life and light stability of the device.[166] Organic HTLs were introduced to prevent oxygen and sulfur diffusion, resulting in stability enhancement (Fig. 13(f)–(h)).[57]

Inorganic encapsulation-based strategies for achieving higher stability have also been reported. A stack of inorganic thin films has been proven to make devices more stable, which is valid in CQD-SCs.[167] A TeO_2 capping layer was deposited on a full device, which effectively prevented the penetration of oxygen and humidity.[146] Similarly, an MgF_2 capping layer was deposited on a full device, resulting in a significant enhancement in the device stability.[147]

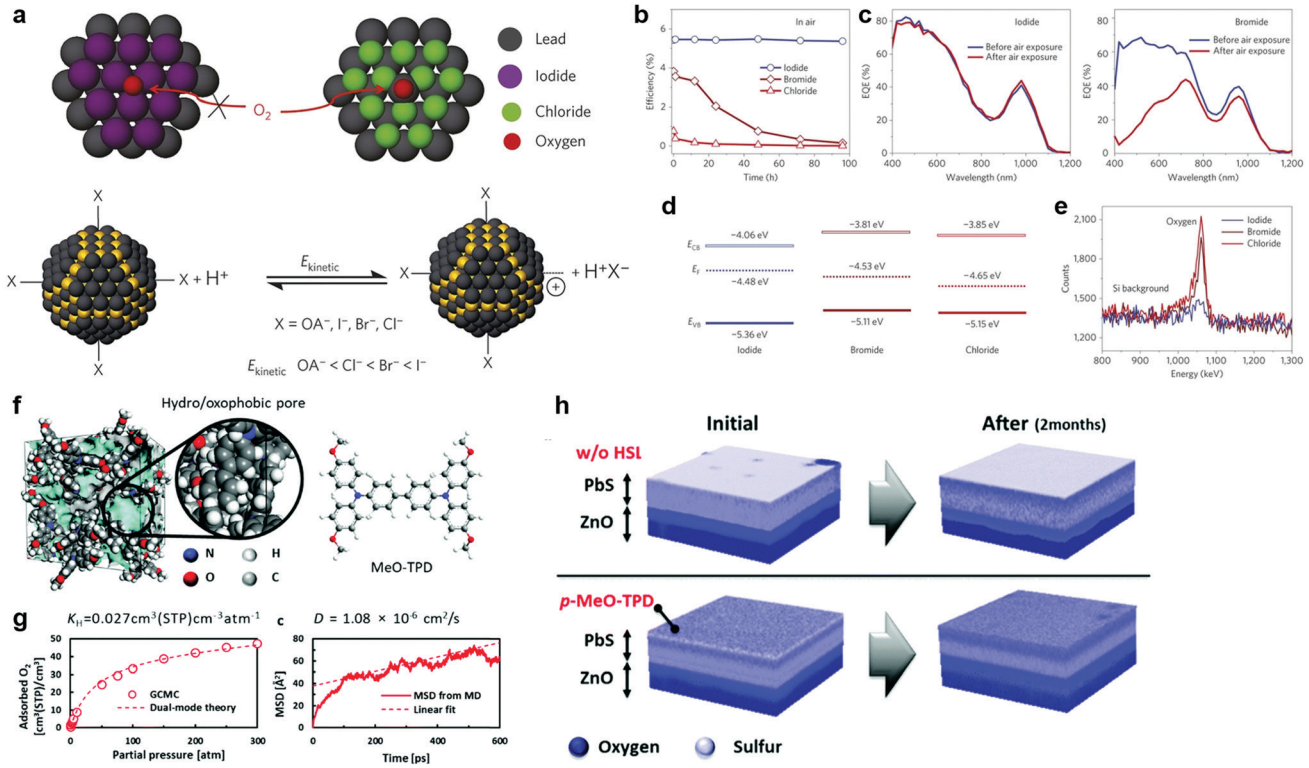

Fig. 13 Strategies to improve the stability of CQDs. (a) Iodide ligand exchange successfully passivates the dangling bonds on CQD surfaces, inhibiting oxygen penetration. The origin of iodide-ligand based defect passivation comes from the high reaction kinetic energy of iodide. (b) PCE comparison between different halide ligand exchange processes. The iodide ligand exchanged device shows much higher stability over other devices using halide ligands. (c) The iodide-processed CQD-SC shows no EQE difference before and after air exposure. The bromide-processed CQD film was oxidized after exposed to air, resulting in a significantly reduced EQE after exposure of the device to air. (d) The iodide ligand exchanged CQD film maintains n-type characteristics, whereas other halide-processed CQD films become p-type following oxidation. (e) Rutherford backscattering spectrometry confirms that iodide-processed CQDs are resistive at oxidation. Reproduced with permission from ref. 38. Copyright 2014, Springer Nature. (f) Schematic of a hydro/oxophobic pore structured HTL. (g) The oxygen permeability as a function of partial pressure and the diffusion constant of entrapped oxygen from MD simulations. (h) The 3D depth profiling of TOF-SIMS. Reproduced with permission from ref. 57. Copyright 2018, the Royal Society of Chemistry.

The shelf lives of CQD-SCs have been continuously investigated and improved, exhibiting high stability over 5 months.[35] However, the device stability under illumination conditions is insufficient and needs to be improved. The photostability of devices could be improved by understanding the interaction mechanisms between the CQDs and adjacent interlayers. To date, many photostability-related reports regarding ZnO modification have been presented, as discussed in this section. These reports imply that much room remains in improving ZnO to realize a higher photostability. Moreover, eventually, a light-robust ETL or an improved CQD-SC structure will be needed.

4. Manufacturing

4.1 CQD film formation

Transformation of CQD solutions to solid films is key to achieving QD-based optoelectronic devices. Since the absorption of incident photons is one of the main determining factors of the efficiency of QD-SCs, the formation of a thick and uniform CQD film through various solution-based methods has been extensively studied. In addition, recombination losses must be minimized and charge extraction to the electrodes must be optimized. For instance, the mean distance between dots should be minimized to enhance the electrical properties of CQD-SCs.[94,168,169] As mentioned in Section 2, short ligands are widely adopted on the CQD surface to realize the preferential transport of photogenerated carriers. Regarding these factors, three major solution-based approaches, drop casting, spin coating, and dipping, have been mainly employed in CQD-SC fabrication on the lab scale (Fig. 14). In this chapter, the progress on film fabrication methods, including strategies for realizing large-area films, is presented.

4.1.1 Drop casting. Drop casting is the simplest method for forming lab-scale small-sized solid QD films. A liquid solution drop is spread over the target area, and the solvent completely evaporates. Compared with other solution-based film formation methods, the drop casting process is very simple yet good for decreasing material waste. In addition, solvent engineering of the CQD solution enables the formation of a thick film with a single drop. Fischer *et al.* successfully developed stable CQD ink and demonstrated CQD-SCs employing the drop casting method.[170] Here, 1-thioglycerol-capped PbS QDs were well preserved in dimethyl sulfoxide (DMSO) solvent with a

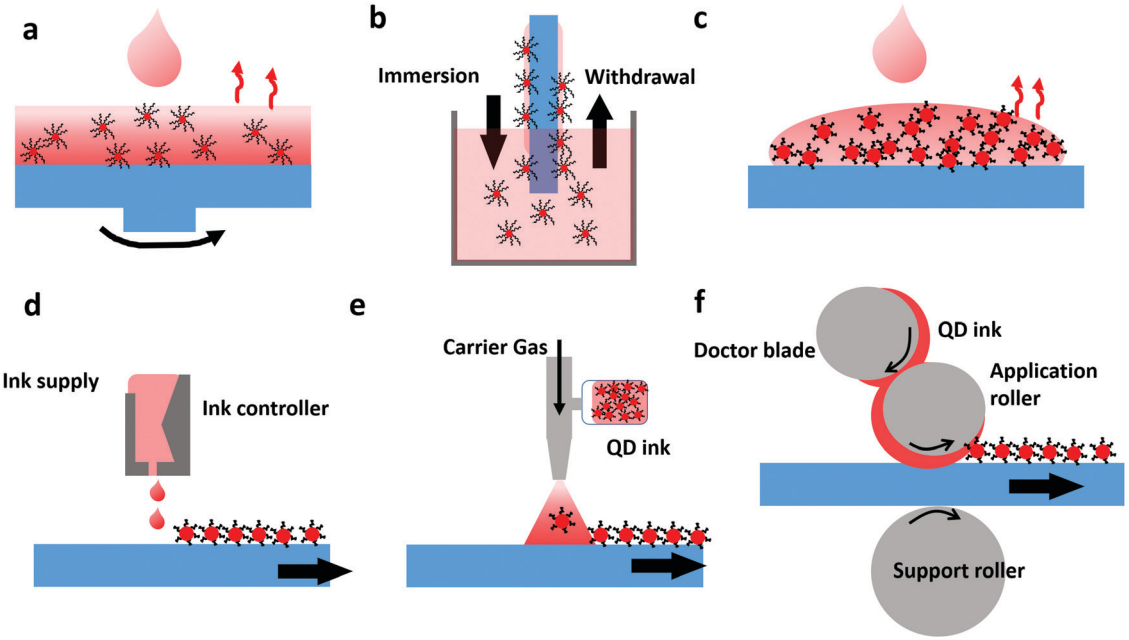

Fig. 14 Various coating methods for CQD SCs: (a) spin-coating, (b) dip coating, (c) drop casting, (d) inkjet printing, (e) spray coating, and (f) doctor blade coating. The long ligand encapsulating the CQD can be substituted for a short one *via* a post-deposition treatment in spin and dip casted films. On the other hand, a pre-treated CQD ink with a short ligand is widely used in drop casting, spray coating, inkjet coating, and doctor blade methods.

pH-adjusting agent. Well-dispersed CQDs in solvent allowed the fabrication of thick CQD films using the drop casting method. According to the study, the consumption of materials used to form the CQD film significantly decreased (1/40) in the drop casting method (0.88 g m^{-2}) compared to the layer-by-layer coating method (38.75 g m^{-2}), as shown in Fig. 15. Moreover, a 200 nm QD film was achieved *via* single drop casting process in this work. Despite simple processes with reduced material consumption, the drop-cast devices show limited PV performance because of their poor film conditions induced by the non-uniform evaporation of the solvent and non-controllable nanomorphology of the active layer.[52,172] As a result, possible solvents for CQD synthesis are limited, and the use of additives for dispersion is inevitable in the drop casting approach.[170,173]

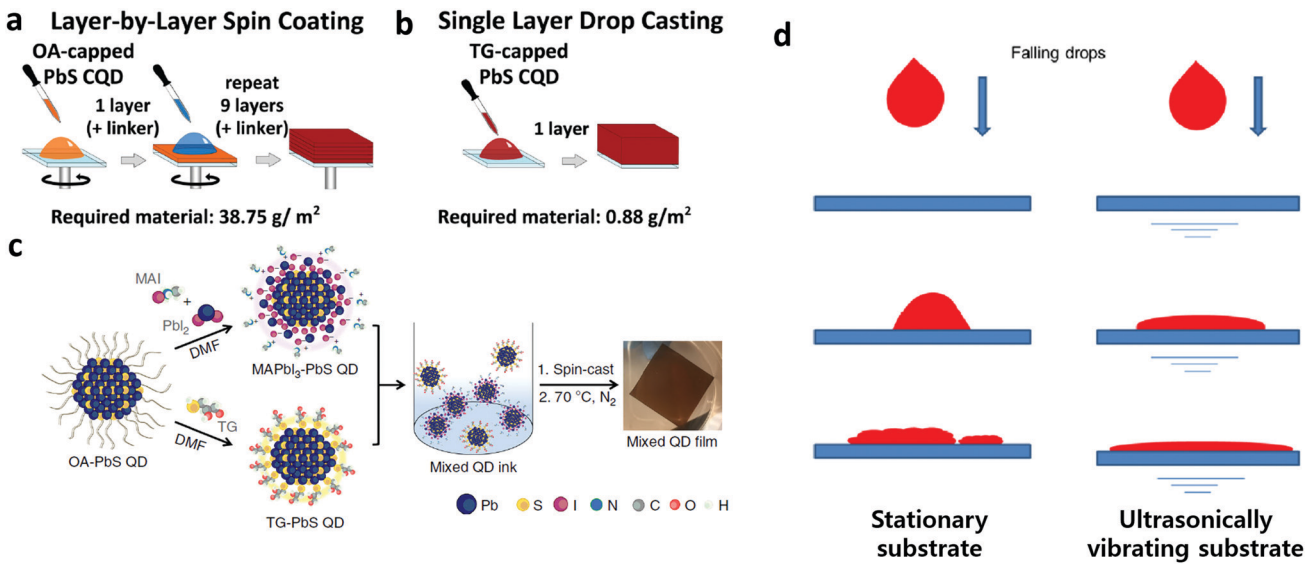

Fig. 15 (a and b) Comparison of CQD ink consumption in the forming of a thick film through spin coating and drop casting. Here, thioglycerol (TG) and oleic acid (OA) were used for dispersing the CQDs in solvents. Reproduced with permission from ref. 170. Copyright 2013, Wiley. (c) Pre-mixed CQD ink capped by TG and methylammonium lead triiodide ($MAPbI_3$). The pre-mixed ink enables us to control carrier transport in the CQD film by modifying the nano morphology of film. Reproduced with permission from ref. 52. Copyright 2017, Springer Nature. (d) Ultrasonic substrate vibration-assisted drop casting for the fabrication of solution processed light harnessing semiconductors. Reproduced with permission from ref. 174. Copyright 2015, Springer.

To achieve better film quality and superior performance of the device, several modifications of the drop casting method have been conducted. With the assistance of substrate vibration, the morphology of the CQD films was made smoother, as proven in perovskite films and SCs.[174] Additionally, control of the mixing ratio between PbS QDs capped by different ligands has been shown to improve the carrier transport balance in the drop-cast film, as shown in Fig. 15.[52] It was found that the miscibility among CQDs capped with different ligands affects the carrier extraction balance. Although the reported PCE of the drop-cast CQD-SC is very low (2.1%) currently, basic studies on ink preparation and film formation for drop-cast CQD layers will provide valuable guidelines for the mass production of CQD-SCs based on simple, high-throughput processes.

4.1.2 Spin and dip coating. Spin and dip coating methods are mostly adopted in CQD-SC research since they are good for small-scale and batch-driven films. In the spin coating method, a CQD solvent is spread on a glass or flexible substrate and changes into a thin film through the high-speed rotation of the substrate. While the substrate rotates, the low-boiling solvent evaporates, and the solid QD film is cast (Fig. 14(a)). In contrast, in the dip coating approach, the substrate is immersed into a CQD solution. By dipping and withdrawing the substrate, a thin layer of QDs is deposited on the target substrate, while the solvent evaporates.[21,175] In comparison to the spin-coated film, the material consumption is significantly reduced for the dip-coated film. Since the size of the equipment for spin and dip coating is sufficiently small enough to fit into an inert gas-filled glove box and/or closed system, these approaches are suitable for evaluating the full potential of materials by isolating CQD films from oxygen or humidity.[71,176,177] As these approaches are also less dependent on solvent than drop casting, CQD-SCs have been developed using various solvents, including toluene, dimethylformamide (DMF), hexane, and so on.[46,178] Moreover, the attainable advantage of the spin and dip coating methods is the easy tunability of the thickness of the deposited film by controlling the number of repeated processes, which may be considered a type of layer-by-layer (LBL) deposition.[39,71,175,179] Furthermore, LBL-based coating and dipping methods are very suitable for exchanging long ligands, passivating CQDs with short ones during the process. To maintain the uniform distribution of CQDs and suppress their aggregation in the solution state, CQDs are normally capped with long ligands, such as oleic acid (OA). However, this long ligand acts as a barrier for charge transport among QDs.[168,180,181] Thus, the inter-dot distance must be decreased to improve the performance of CQD-SCs. As a physical approach, external pressure can be used to compact the QD active layer by removing voids, which results in improved carrier transport and device performance.[94] In contrast, in chemical ligand exchange approaches, long ligands are substituted by short ligands after the surface modification and washing steps of the LBL process. Depending on the polarity of the exchanged ligand, the carrier transport inside the film can be controlled.[11] In particular, PbS or PbSe CQDs can form either an n- or p-type active layer *via* the introduction of TBAI and EDT ligands, respectively.[27,35,44,99] By introducing different short ligands during the modification step of the LBL process, a p–n structure active layer can be utilized with the same set of CQDs, which enables directional control of the photogenerated carrier. In addition, a mild washing solvent (*e.g.*, acetonitrile) reduces the defects on the QD surface during the LBL washing process, thereby resulting in reduced recombination losses and higher device performance.[36,60] As a result of these developments, record-breaking efficiencies have been reported mainly in devices using the spin and dip coating approaches.[18,54]

4.2 Upscaling methods

While many solution-based approaches for CQD-SCs have been successfully developed, most of them have been conducted with small-sized substrates using lab-scale systems. Unfortunately, uniformity and sufficient thickness over a large area are difficult to achieve using these film formation techniques. Reduction of material consumption is a big challenge for dip- and spin-coating approaches. LBL-based thick films are not suitable for mass production due to their lengthy processing, consisting of multiple deposition and washing steps. Additionally, the drop casting method requires careful handling of the solvent to achieve uniform films. Thus, a single-step deposition method in which the thickness and uniformity of QD films can be controlled is desirable for mass production. For example, a Canadian CQD-SC company, QD solar Inc., have focused on forming QD films from a single step method for fabricating devices *via* a roll-to-roll process. By employing pre-ligand-exchanged CQD inks, thick and uniform QD films have been demonstrated despite several challenges, such as poor colloidal stability, use of high-boiling-point solvents for CQD dispersion, and so on.[52,171,182] Three common single-step approaches for constructing QD-based optoelectronic devices are inkjet printing, spray coating, and slot-die coating, as shown in Fig. 14. The properties of each method are summarized and compared to those of lab scale processes in Table 3. The advantage of these approaches is the ability to fabricate devices with reduced material consumption in a short time. The current status of each deposition method will be addressed.

An inkjet printing system can be used to deposit expensive materials with reduced material consumption over a target area. Thus, this method is widely used for solution-based electrically functional materials. Using multiple nozzle heads, which cover the entire substrate, a large-area film can be easily deposited within a certain time. Moreover, the film uniformity can be controlled by modifying the solvents. However, the coffee-ring effect caused by the uneven evaporation rate of the solvent in the ink deteriorates the uniform performance of the CQD-SCs. The introduction of a mixed solvent for the QDs leads to reduced surface tension and viscosity, which enables the fabrication of reproducible flat films.[183] Many inkjet-based PV devices have been developed because of their excellent film quality and acceptable film deposition process for large-sized films.[184–186] However, to date, most studies on inkjet-printed CQD optoelectronic devices have focused on LEDs rather than PV cells, since complicated patterned light-emitting layers are necessary for full-colour devices. To date, inkjet-printed LEDs have been

Table 3 Comparison of different deposition techniques for CQD-SCs

Methods	CQD consumption	Thickness control	Process speed	Examples of reported PCEs	Ref.
Spin coating	Very high	Good	Low	13.4% ($CsPbI_3$)	54
Dip coating	High	Good	Low	10.6% (PbS)	58
Drop casting	Moderate	Poor	Moderate	2.1% (PbS)	170
Inkjet printing	Low	Good	High	—[c]	
Spray coating	Low or moderate[a]	Moderate or poor	High	8.1% (PbS)	171
Doctor blade coating	Low	Good	High[b]	10.0–10.3% (PbS)[d]	2 and 55
Slot-die coating	Low	Good	High		

[a] Depending on the spray system, the consumption may be varied. [b] According to polymer solar cell results, the speed of the doctor blade approach is around 15 mm s^{-1}. [c] Inkjet-based CQD-SCs have been barely reported. [d] CQD ink for doctor blade coating is compatible with the slot-die method without further modification.

successfully commercialized, and the infrastructure and facilities for inkjet processed CQD films are ready for mass production by materials (Nanosys QD vision, Nanoco and so on), device (Samsung Electronics, TCL, BOE), and manufacturing equipment companies (Kateeva, Epson). Consequently, the feasibility of producing large inkjet-based CQD-SCs is very promising.

The spray coating technique is a film deposition method based on the collection of small liquid drops dispersed in a carrier gas. A CQD solution is sprayed through a nozzle using high pressurized gas. All processes can be performed under ambient conditions; thus, the use of an inert gas-filled glove box is not essential in this approach. Uniformly deposited, large-sized CQD films have been achieved by simply controlling the nozzle and gas pressure.[187,188] The thickness of the CQD film is controllable through a repeatable process, as shown in Fig. 16. Hence, spray coating of CQDs paves the way for forming large-sized, low-cost films. The key issue of the spray coating method is how to uniformly disperse CQDs in the carrier gas and maintain their function. To achieve better film quality, long ligand-capped CQDs are normally dispersed in a solvent. Then, the pressurized inert gas forces the CQDs to move and deposit on the substrate. After that, the ligand is exchanged for a short ligand to boost carrier transport among nanocrystals. A comparison of spin- and spray-coated films indicates that the surface of the spray-coated layer is smoother.[40] In addition, pinholes and defects are significantly suppressed in spray-coated films, resulting in an increased minority carrier lifetime and an enhanced diffusion length of the CQDs. These benefits have led to a uniform performance of CQD-SCs fabricated *via* spray coating (PCE of 8.1 ± 0.7%). In addition, the possibility of a roll-to-roll process *via* spray coating has also been verified with flexible substrate-based SCs.[171]

The last possible upscaling method is doctor blade or slot-die coating, which is widely accepted in the industry for large-area films with reduced material consumption. Using a large dispenser head and a knife, a uniformly coated layer can be achieved in slot-die and/or doctor blade coating.[189] The amount of ink can be controlled by modifying the head of the slot-die coater and knife of the doctor blade coater, which enables the deposition of a film with the desired thickness. Moreover, this process is compatible with a cost-efficient roll-to-roll process. Utilizing these advantages, many research groups have successfully demonstrated slot-die- or doctor blade-processed SCs with solution-processed light absorbers, including chalcogenides, perovskites and organic materials.[190] CQDs are also soluble materials; thus, attempts have been made to realize large-area films using these techniques.[2] According to Kirmani *et al.*, the introduction of a slot-die-coated film results in significantly reduced materials consumption (only 4%) compared to a film deposited *via* a spin coating method.

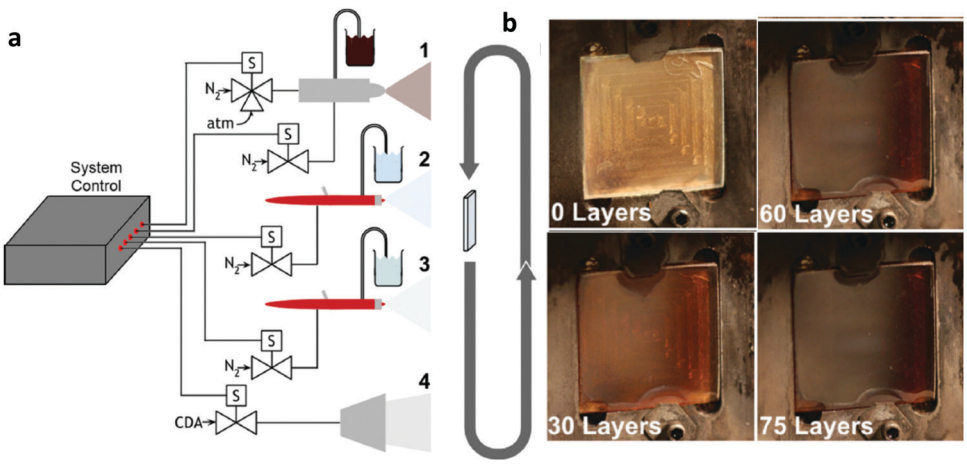

Fig. 16 (a) Schematic of a spray coating system for producing a CQD film, (b) Image of CQD films with different numbers of sprayed layers. Reproduced with permission from ref. 40. Copyright 2015 Wiley.

In addition, ambient humidity and oxygen can act as dopants of the CQD ink in slot-die coating, leading to enhanced electrical properties of the films with these dopants, as introduced in Section 2. By employing a high-speed coating process, meeting industrial requirements (>15 m min^{-1}), a PCE of 10.3% was obtained. A summarized comparison of the different deposition techniques for CQD-SCs is presented in Table 3. As of now, doctor blade or slot-die coating techniques seem the most promising for mass production. Further intensive studies on enlarging CQD films will result in commercially available devices.

5. Obstacles for CQD-SC commercialization

5.1 Economic viability of CQD-SCs

Commercially available c-Si SCs and their modules are dominant technologies for utility-scale PV power plants. Their market share exceeds 95% owing to their high efficiency ($>20\%$ module efficiency) and low cost (~ 0.2 \$ per W). Moreover, the output of a c-Si PV module system degrades by less than 20% after 20 years of operation. As a result, the cumulative installation of c-Si SCs is over 500 GW.[194] In addition, more than 2.5% of the world's electricity generation is from c-Si PV modules. However, the thick glass sandwich c-Si PV module is too heavy (>16 kg m^{-2}), which limits its application (*e.g.*, building- or vehicle-integrated PV modules). Moreover, rigid c-Si PV modules are generally not compatible with portable devices. Although the annual demand for non-utility-type PV modules (portable, aerospace, vehicle-integrated, and microstructure-integrated products) is predicted to be less than 100 MW, representing only 0.1% of the utility-scale market, this market is growing much faster than the heavy and rigid c-Si PV market.[191] This niche market will be an opportunity for thin film-based SCs to enter the commercialized market. Compared to the utility-scale PV market, the functionality of solar modules, such as their light weight (W kg^{-1}), design, and flexibility, plays a very important role in this area. The projected cost of the emerging flexible PV modules is approximately higher than 1 \$ per W, as shown in Fig. 17(a).

Fortunately, CQD-SCs meet the requirements of the niche PV market. Some pioneering research studies have systematically analysed the attainable flexible CQD-SC cost from the viewpoint of elements and processes. Currently, the estimated lowest cost for flexible PbS CQD-SCs is 0.94 \$ per W, as shown in Fig. 17(b).[192] Here, the efficiency of the CQD-SC (PET film/indium zinc oxide (IZO)/ZnO/PbS/NiO_x/Al) is assumed to be 19%, and the device is assumed to be manufactured *via* a roll-to-roll process. According to the data, the synthesis method using $PbCl_2$ and thioacetamide precursors suggested by Huang *et al.* significantly decreases labour as well as material costs (0.16 \$ per W).[195] However, the additional cost of PbS CQD ink preparation for slot-die coating (0.11 \$ per W) is inevitable in the absorber preparation.[101] Finally, common elements for the substrate (0.11 \$ per W), buffer layer (0.07 \$ per W), reliable

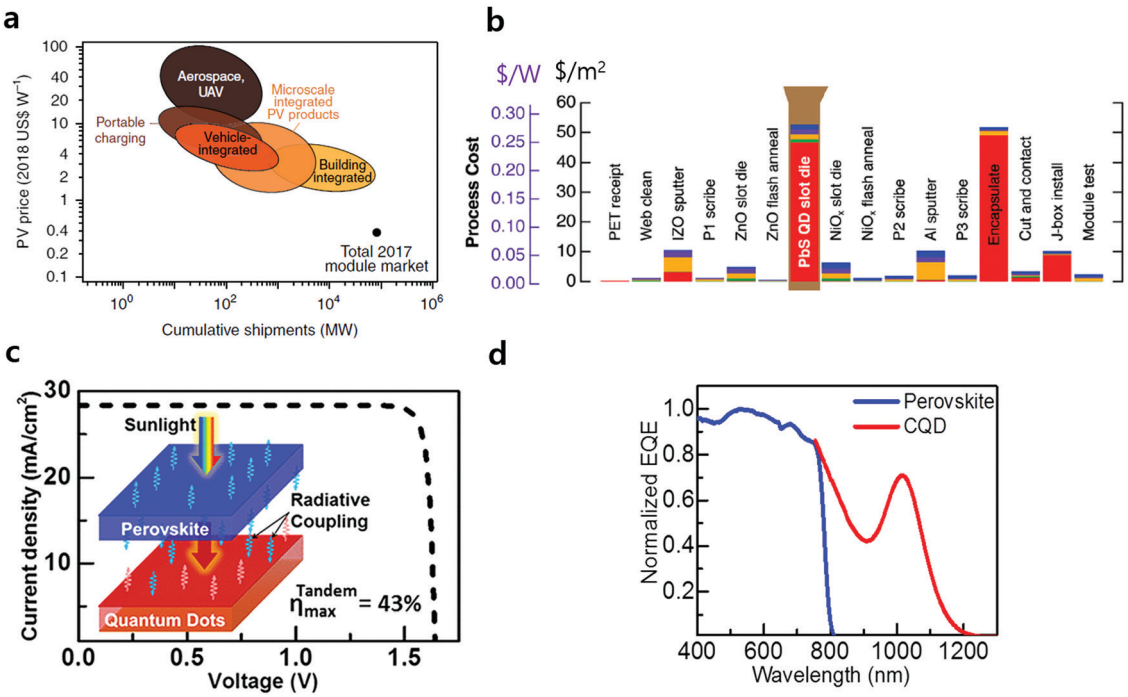

Fig. 17 (a) Projected emerging PV market size as a function of the PV price per watt. Reproduced with permission from ref. 191. Copyright 2018, Springer Nature. (b) Manufacturing cost for a roll-to-roll processed PV module with flexible substrate (100 μm thick PET film). The projected total cost is 0.94 \$ per W. Here, it is assumed that the efficiency of the PbS CQD PV module is 19%. Reproduced with permission from ref. 192. Copyright 2018, the Royal Society of Chemistry. (c) c-Si and low band gap CQD tandem cell structure with its theoretically calculated *I*–*V* curve and (d) external quantum efficiency under AM 1.5 G conditions. Reproduced with permission from ref. 193. Copyright 2018, the American Chemical Society.

device (encapsulant, 0.27 $ per W) and circuit (electrode, contact and junction box, 0.15 $ per W) may increase the cost of PbS-CQD PV modules. The common price for roll-to-roll-based SCs still has room for improvement in the high volume market. In addition, the cost of QD ink will be reduced by implementing solvent recycling, developing a robust synthesis method, and automating the process. Further progress in the substrate, encapsulant and CQD ink would accelerate the commercialization of CQD-SCs in the near future.

Another strategy to commercialize CQD-SCs is a tandem approach. As mentioned above, the current cost of a c-Si PV module is approximately 0.2 $ per W, which is almost impossible to reach using CQDs as an absorber in SCs, considering the current status.[196] Hence, many companies and research institutes, such as Ubiqd, QD Solar Inc., Los Alamos National laboratory, Caltech, and so on, have tried to find a way to boost the performance of c-Si SCs with the assistance of specially designed QD films and devices.[189,197–199] Because of the thermodynamic (Shockley–Queisser) limit of light-harvesting materials, the optimized E_g of the active layer for conventional SCs is approximately 1.1 eV.[126,200] For instance, the E_g values of Si, chalcogenides (CIGS), GaAs, CdTe, and perovskites, which are widely used in conventional SCs, are in the range of 1.1–1.5 eV. As a result, low energy photons, below the E_g (wavelength $>$ 1100 nm), penetrate the cell and do not contribute to the photocurrent in conventional SCs. The total energy of non-absorbed photons is 16.4 mW cm^{-2} in conventional single c-Si SCs under AM 1.5 G solar irradiation.[201,202] Thus, many research groups have developed small E_g PbS-incorporated SCs and proposed tandem structures consisting of conventional top cells and PbS bottom cells (see Fig. 17(c) and (d)). Since lattice matching among light-absorbing films is not necessary in solution-processed devices, a small E_g CQD-SC is versatile for a tandem device. Although the cost of the cell itself increases upon implementing a CQD bottom cell, the enhanced performance of the tandem cell with the stacking of a conventional device and IR-converting CQDs curtails its levelized cost of electricity.

The energy attainable by introducing a small E_g CQD cell into the tandem structure was theoretically calculated based on experimental results. According to the calculation, the PCE of a tandem cell with a stack of CdTe (E_g = 1.5 eV) and IR-absorbing CQD (E_g = 0.75 eV) cells reaches over 40%.[90] Moreover, by harnessing solar light in the IR region, a PCE of 29.7% is expected in a monolithic tandem device with perovskite (E_g = 1.55 eV) and PbS CQD (E_g = 1.0 eV) cells.[193] Comparing certified state-of-the-art perovskite (25.2%) and CQD (16.6%) SCs, more progress is projected in tandem devices. To realize a highly efficient tandem structure with a conventional device, improvement in the performance of the bottom cell, consisting of small E_g CQDs, is essential. Y. Bi *et al.* empirically demonstrated a 7.9% efficiency single PbS CQD-SC, the E_g of which is below 1.0 eV.[203] In particular, the EQE of the cell is over 80% at 1350 nm. With the assistance of extended photon absorption up to 1400 nm, achieved by attaching bottom PbS CQD cells, efficiencies of 3.33 and 0.67% were added to the top perovskite (long pass 750 nm) and c-Si (long pass 1100 nm) SCs, respectively. According to the roadmap of QD solar Inc., an improvement of more than 4% will be achieved by inserting CQD-SCs at the bottom of c-Si SC systems.[204] Moreover, optimization of the optical structure is projected to lead to better performance of small E_g CQD-SCs located under conventional cells. A selective cavity mirror consisting of multiple layers of an oxide and a nitride reflects IR light, which allows small E_g CQDs to convert more photons to a current.[205] Although further studies are required to improve the stability, interlayer, and optical design, the stacking of a conventional solar absorber and low E_g CQDs provides an opportunity to successfully overcome the Shockley–Queisser limit of a single junction cell.

5.2 Eco-friendly SCs

To date, highly efficient devices based on Pb-containing CQDs, such as PbS (PCE of 12.1%) and $CsPbI_3$ (14.1%) nanocrystals, have been reported. However, the use of toxic elements, including Pb, Hg, Cd, and so on, severely restricts their usage in nearly all commercial electronic devices. Many regulations have been imposed on the amount of Pb that can be used.[209] Moreover, end-of-life issues need to be addressed for PV modules containing Pb-based CQDs. Although the Pb-based active layer is very thin (hundreds of nanometres), the amount of accumulated Pb from MW- and/or GW-sized CQD PV systems is non-negligible. c-Si PV modules, which currently dominate the PV market, also face similar problems. Due to environmental regulations, replacement of Pb-containing solders (SnPb) with eco-friendly solders and collection of these solders from aged modules have been intensively studied.[210] As Cd-containing CQDs have been successfully substituted for heavy metal-free (InP, CIGS, and so on) ones in commercialized CQD displays, the development of highly efficient CQD-SCs with non-toxic materials is expected.[211–213] Unfortunately, the performance of CQD-SCs with eco-friendly elements is currently inferior to that of PVs with PbS CQDs, as summarized in Table 4. However, progress in new materials and device structures would enable the efficient utilization of CQD devices with heavy metal-free elements.

Among the many possible non-toxic materials, In-based binary and ternary (InAs, InSb, InZnP) QDs have been investigated, which can convert a broad range of solar light (from UV to NIR) into electricity. In-based nanocrystals and their films exhibit excellent optical and electrical properties for optoelectronic devices. Their absorption coefficients are very high such that an film of only 100 nm is sufficiently thick enough to absorb incident photons.[214,215] Moreover, the electron mobility of films with InAs CQDs exceeds 15 cm^2 V^{-1} s^{-1} in field-effect transistors.[216]

Table 4 Efficiency thin-film photovoltaic cells with toxic and non-toxic CQDs

Materials		PCE (%)	Ref.
Pb based QDs	PbS CQD	12.1	18
	$CSPbI_3$	14.1	66
Non-toxic QDs	InZnP	1.2	206
	$AgBiS_2$	6.3	207
	$CuInS_2$	1.2	208

In addition, the attainable advantage of In-based eco-friendly CQDs is the enhanced MEG, because their CM threshold is near $2E_g$.[217] Moreover, In-based QDs show excellent stability under high voltage field, as reported by Samsung Electronics.[218] Despite the excellent optical and electrical properties of In-based CQDs, the reported efficiencies of solid-state SCs with 3.2 nm InP and 2.8 nm InZnP CQDs are only 0.7 and 1.2%, respectively.[206] This result can be mainly attributed to the poly-dispersity of the CQD size and increased recombination losses induced by poor CQD surface passivation.[219,220] For the better performance of In-based CQD SCs, these issues should be overcome. Meanwhile, implementation of In-based CQDs in SCs as a buffer layer rather than an active layer has been suggested. As the In-based nanocrystal layer exhibits very high mobility, the incorporation of an In-based CQD film into a SC led to improved carrier collection efficiency. Moreover, the E_g of the In-based QD can be tuned by surface treatment, enabling the desired band alignment between the electrode and active layer. Song *et al.* inserted an InAs QD layer between an electrode and a p–n-type PbS QD active layer.[221] The air-stable InAs QD film boosted the carrier collection efficiency, thereby leading to improved FF (0.39 → 0.63), J_{SC} (13.13 → 20.92 mA cm^{-2}), V_{OC} (0.21 → 0.54 V), and PCE (1.1 → 7.2%) values. Although the active layer still consisted of Pb-based CQDs, this work revealed that surface-treated InAs QDs have the potential to realize eco-friendly CQD-SCs.

Other possible candidates for non-toxic CQD-SCs are Ag- and Sb-based compound nanocrystals (Sb_2Se_3, Ag_2S, $AgBiS_2$, $AgBiSe_3$). The bulk E_g values of these materials are narrow, so they can absorb a wide range of IR light (*i.e.*, bulk E_g of $AgBiS_2$: 1.1 eV, Ag_2S: 1.07 eV, Ag_2Se: 0.17 eV, Sb_2Se_3: 1.0 eV).[207,222,223] As a result, intensive studies have been conducted on developing SCs using these bulk materials. Solid thin-film SCs with a bulk Sb_2Se_3 layer have shown promising efficiency (PCE of 7.5–9.2%).[224,225] This result was achieved without incurring high costs (In and Ga) or using toxic (Cd and Pb) materials. However, the excellent properties of bulk Sb_2Se_3 have not been linked to a highly efficient CQD-SC because of its poor size control and corrosion during the synthesis process.[223] Regardless of the many obstacles for realizing highly efficient non-toxic CQD-SCs, such as the poor understanding of the CQD surface passivation, charge transport inside the film, and CQD composition, a record high PCE of 6.31% has been achieved using $AgBiS_2$ QDs.[207] The E_g of $AgBiS_2$ lies between those of ZnO and the p-type polymer layer; thus, the introduction of an ETL and an HTL boosts the photogenerated carrier collection efficiency in $AgBiS_2$ CQD-SCs. Further modification of the surface passivation and size control of Ag- and Sb-based CQDs is predicted to help overcome the limitations of their devices by minimizing recombination losses and maximizing light absorption.

Last, CQDs consisting of chalcopyrite (*e.g.*, $CnInGaSe_2$) have also been considered as non-toxic alternatives. For the bulk film, the record efficiency of a Cu-In-Ga-Se SC has exceeded 20%, and this cell is competitive with other thin-film and c-Si PV cells in the commercial market.[226] Because of the strong absorption coefficient and the possibility of tuning the E_g, chalcopyrite CQD optoelectronic devices have been intensively studied.[227] However, the studies have mainly been focused on dye-sensitized SCs rather than on solid-type SCs owing to inefficient charge transport in the CQD film. The delocalized ions and Cu vacancies in chalcopyrite CQDs contribute to broadening of the CB and VB, which act as trap sites in the solid film.[228,229] In particular, the intra-gap state dramatically decreases the carrier mobility. As a result, a PCE of only 1.1% has been achieved in solid-type chalcopyrite CQD-SCs, while the certified PCE of dye-sensitized-type chalcopyrite CQDs is 11.6%.[208,227] Since thermal annealing of films and control of elements may reduce the defect states of chalcopyrite CQDs, control of the carrier transport inside the chalcopyrite CQD film is necessary for developing solid-type SCs based on this.

6. Conclusion and remarks

CQD-SCs are considered to be strong candidates as next-generation energy sources. By utilizing the quantum confinement effect, efficient colour-tunable SCs with varying CQD sizes can be fabricated. Along with the improvements that have been achieved in CQD materials and surface chemistry over the last decade, many studies have focused on enhancing the PV performance of the devices. The development in device engineering has led to an enlarged depletion region and efficient charge extraction of photogenerated charges, achieving a certified PCE of over 16%. CQDs exhibit several advantageous features compared to competitive emerging PV materials: (1) control of E_g by tuning the CQD size, (2) energy level alignment *via* surface treatment, (3) low MEG threshold, (4) utilization of infrared light, and (5) possible use of air-stable inorganic materials for all device layers. Moreover, CQDs exhibit high feasibility for film deposition *via* solution processes. Industrial film deposition methods, such as inkjet printing, doctor blading and slot-die coating, can be used in CQD film deposition. Furthermore, post-treatment (high-temperature annealing) would not be required for CQD film deposition. The most competitive emerging PVs, perovskites, require a very fine film quality to achieve a high PCE. The anti-solvent dripping process (which is essential for the fine film quality) during the spin coating of a perovskite solution is a large bottleneck in the upscaling process. Another possible candidate for competitive emerging PVs is organic photovoltaics (OPVs). The reported high-efficiency OPVs have very high costs associated with the synthesis of the polymers. Thus, CQD-SCs are one of the most promising candidates for next-generation PVs. CQD-SC are expected to enter the flexible, portable PV market in the near future. Moreover, stacks of conventional (c-Si or thin-film) SCs and low E_g CQD-SCs can overcome the efficiency limit of a single cell. However, some issues should be addressed for the successful commercialization of CQD-SCs.

The most urgent issues to be handled are the device stability and environmental toxicity of the materials. The operational lifetime of the devices under illumination is only 1100 h at the T_{80} point. If proper device encapsulation excludes other environmental degradation sources, such as oxygen and humidity,

then the remaining unsolved issue will be improving the stability of the light-unstable parts in the CQD devices. The hydroxide components on the CQD surfaces should be effectively passivated *via* ligand exchange or surface treatments. Replacement or passivation (doping) with light-stable materials of the most widely used light-unstable ETL, ZnO, is required. To date, metal doping of ZnO has exhibited the most effective defect passivation characteristics, but not enough to satisfy commercial standards. Additionally, the interfacial junctions between each PV constituent layer should be carefully investigated. The defect states at these junctions could act as non-radiative recombination centres during operation under illumination.

The highest-performing CQD-SCs consist of Pb-included elements, which are strictly regulated for commercial usage. Although the total amount of Pb for a single device is almost negligible, the amount would be considerable when the single devices are integrated into PV modules. Less toxic candidate materials, such as In, As, or Sb, have been investigated to achieve eco-friendly and efficient CQD-SCs. However, the difficulties associated with CQD size control or in the synthesis processes need to be overcome for these materials. Although non-Pb-based CQD-SCs have shown a maximum PCE of only ~6%, they have been reported to exhibit promising characteristics, such as high mobility and absorption coefficients. Thus, further investigation of these materials to realize eco-friendly and efficient CQD-SCs would be very promising.

Once the outstanding advantages of CQDs can be effectively utilized in device physics and materials science, commercialization of CQD-SCs will no longer be uncertain, and CQD-SCs will make up a portion of the future PV market.

Conflicts of interest

There are no conflicts to declare.

Acknowledgements

This work is supported by the National Science Foundation (NSF, grant no. 1808163). Hyung-Jun Song acknowledges the New & Renewable Energy Technology Development Program of the Korea Institute of Energy Technology Evaluation and Planning (KETEP) grant, funded by the Ministry of Trade, Industry and Energy, Korea (No. 20193010014570) and the National Research Foundation of Korea (NRF) through the Basic Science Research Program (NRF-2019R1F1A1057693).

References

1 A. Kongkanand, K. Tvrdy, K. Takechi, M. Kuno and P. V. Kamat, *J. Am. Chem. Soc.*, 2008, **130**, 4007–4015.
2 A. R. Kirmani, A. D. Sheikh, M. R. Niazi, M. A. Haque, M. Liu, F. P. G. de Arquer, J. Xu, B. Sun, O. Voznyy, N. Gasparini, D. Baran, T. Wu, E. H. Sargent and A. Amassian, *Adv. Mater.*, 2018, **30**, 1801661.
3 C. R. Kagan, E. Lifshitz, E. H. Sargent and D. V. Talapin, *Science*, 2016, **353**, aac5523.
4 H. J. Jang, J. Y. Lee, J. Kwak, D. Lee, J.-H. Park, B. Lee and Y. Y. Noh, *J. Inf. Disp.*, 2019, **20**, 1–8.
5 Z. Hens and I. Moreels, *J. Mater. Chem.*, 2012, **22**, 10406–10415.
6 J.-S. Lee, M. V. Kovalenko, J. Huang, D. S. Chung and D. V. Talapin, *Nat. Nanotechnol.*, 2011, **6**, 348.
7 J.-H. Choi, A. T. Fafarman, S. J. Oh, D.-K. Ko, D. K. Kim, B. T. Diroll, S. Muramoto, J. G. Gillen, C. B. Murray and C. R. Kagan, *Nano Lett.*, 2012, **12**, 2631–2638.
8 M. Nam, S. Kim, S. Kim, S.-W. Kim and K. Lee, *Nanoscale*, 2013, **5**, 8202–8209.
9 H. Lee, J. Lim, J. Song, H. Heo, K. An, J. Kim, S. Lee, K. Char, H.-J. Song and C. Lee, *Nanotechnology*, 2018, **30**, 065401.
10 S. Lee, J. C. Flanagan, J. Kim, A. J. Yun, B. Lee, M. Shim and B. Park, *ACS Appl. Mater. Interfaces*, 2019, **11**, 19104–19114.
11 S. J. Oh, Z. Wang, N. E. Berry, J.-H. Choi, T. Zhao, E. A. Gaulding, T. Paik, Y. Lai, C. B. Murray and C. R. Kagan, *Nano Lett.*, 2014, **14**, 6210–6216.
12 M. J. Speirs, D. N. Dirin, M. Abdu-Aguye, D. M. Balazs, M. V. Kovalenko and M. A. Loi, *Energy Environ. Sci.*, 2016, **9**, 2916–2924.
13 V. I. Klimov, *Annu. Rev. Condens. Matter Phys.*, 2014, **5**, 285–316.
14 O. E. Semonin, J. M. Luther, S. Choi, H.-Y. Chen, J. Gao, A. J. Nozik and M. C. Beard, *Science*, 2011, **334**, 1530–1533.
15 A. Rao and R. H. Friend, *Nat. Rev. Mater.*, 2017, **2**, 17063.
16 D. Hahm, D. Ko, B. G. Jeong, S. Jeong, J. Lim, W. K. Bae, C. Lee and K. Char, *J. Inf. Disp.*, 2019, **20**, 61–72.
17 https://www.pv-tech.org/news/hanergys-new-business-model-is-selling-thin-film-production-lines-to-indust.
18 NREL, Solar Cell Efficiency Chart, available online: https://www.nrel.gov/pv/assets/pdfs/best-research-cell-efficiencies.20191210.pdf, accessed on 10 December 2019.
19 J. M. Luther, M. Law, M. C. Beard, Q. Song, M. O. Reese, R. J. Ellingson and A. J. Nozik, *Nano Lett.*, 2008, **8**, 3488–3492.
20 J. J. Choi, Y.-F. Lim, M. E. B. Santiago-Berrios, M. Oh, B.-R. Hyun, L. Sun, A. C. Bartnik, A. Goedhart, G. G. Malliaras, H. D. Abruña, F. W. Wise and T. Hanrath, *Nano Lett.*, 2009, **9**, 3749–3755.
21 J. M. Luther, J. Gao, M. T. Lloyd, O. E. Semonin, M. C. Beard and A. J. Nozik, *Adv. Mater.*, 2010, **22**, 3704–3707.
22 R. Debnath, M. T. Greiner, I. J. Kramer, A. Fischer, J. Tang, D. A. R. Barkhouse, X. Wang, L. Levina, Z.-H. Lu and E. H. Sargent, *Appl. Phys. Lett.*, 2010, **97**, 023109.
23 A. G. Pattantyus-Abraham, I. J. Kramer, A. R. Barkhouse, X. Wang, G. Konstantatos, R. Debnath, L. Levina, I. Raabe, M. K. Nazeeruddin, M. Grätzel and E. H. Sargent, *ACS Nano*, 2010, **4**, 3374–3380.
24 D. A. R. Barkhouse, R. Debnath, I. J. Kramer, D. Zhitomirsky, A. G. Pattantyus-Abraham, L. Levina, L. Etgar, M. Grätzel and E. H. Sargent, *Adv. Mater.*, 2011, **23**, 3134–3138.
25 J. Gao, C. L. Perkins, J. M. Luther, M. C. Hanna, H.-Y. Chen, O. E. Semonin, A. J. Nozik, R. J. Ellingson and M. C. Beard, *Nano Lett.*, 2011, **11**, 3263–3266.

26 H. Liu, J. Tang, I. J. Kramer, R. Debnath, G. I. Koleilat, X. Wang, A. Fisher, R. Li, L. Brzozowski, L. Levina and E. H. Sargent, *Adv. Mater.*, 2011, **23**, 3832–3837.
27 J. Tang, K. W. Kemp, S. Hoogland, K. S. Jeong, H. Liu, L. Levina, M. Furukawa, X. Wang, R. Debnath, D. Cha, K. W. Chou, A. Fischer, A. Amassian, J. B. Asbury and E. H. Sargent, *Nat. Mater.*, 2011, **10**, 765.
28 A. H. Ip, S. M. Thon, S. Hoogland, O. Voznyy, D. Zhitomirsky, R. Debnath, L. Levina, L. R. Rollny, G. H. Carey, A. Fischer, K. W. Kemp, I. J. Kramer, Z. Ning, A. J. Labelle, K. W. Chou, A. Amassian and E. H. Sargent, *Nat. Nanotechnol.*, 2012, **7**, 577.
29 I. J. Kramer, D. Zhitomirsky, J. D. Bass, P. M. Rice, T. Topuria, L. Krupp, S. M. Thon, A. H. Ip, R. Debnath, H.-C. Kim and E. H. Sargent, *Adv. Mater.*, 2012, **24**, 2315–2319.
30 H. Liu, D. Zhitomirsky, S. Hoogland, J. Tang, I. J. Kramer, Z. Ning and E. H. Sargent, *Appl. Phys. Lett.*, 2012, **101**, 151112.
31 J. Tang, H. Liu, D. Zhitomirsky, S. Hoogland, X. Wang, M. Furukawa, L. Levina and E. H. Sargent, *Nano Lett.*, 2012, **12**, 4889–4894.
32 X. Lan, J. Bai, S. Masala, S. M. Thon, Y. Ren, I. J. Kramer, S. Hoogland, A. Simchi, G. I. Koleilat, D. Paz-Soldan, Z. Ning, A. J. Labelle, J. Y. Kim, G. Jabbour and E. H. Sargent, *Adv. Mater.*, 2013, **25**, 1769–1773.
33 P. Maraghechi, A. J. Labelle, A. R. Kirmani, X. Lan, M. M. Adachi, S. M. Thon, S. Hoogland, A. Lee, Z. Ning, A. Fischer, A. Amassian and E. H. Sargent, *ACS Nano*, 2013, **7**, 6111–6116.
34 Z. Ning, D. Zhitomirsky, V. Adinolfi, B. Sutherland, J. Xu, O. Voznyy, P. Maraghechi, X. Lan, S. Hoogland, Y. Ren and E. H. Sargent, *Adv. Mater.*, 2013, **25**, 1719–1723.
35 C.-H. M. Chuang, P. R. Brown, V. Bulović and M. G. Bawendi, *Nat. Mater.*, 2014, **13**, 796.
36 A. R. Kirmani, G. H. Carey, M. Abdelsamie, B. Yan, D. Cha, L. R. Rollny, X. Cui, E. H. Sargent and A. Amassian, *Adv. Mater.*, 2014, **26**, 4717–4723.
37 Z. Ning, H. Dong, Q. Zhang, O. Voznyy and E. H. Sargent, *ACS Nano*, 2014, **8**, 10321–10327.
38 Z. Ning, O. Voznyy, J. Pan, S. Hoogland, V. Adinolfi, J. Xu, M. Li, A. R. Kirmani, J.-P. Sun, J. Minor, K. W. Kemp, H. Dong, L. Rollny, A. Labelle, G. Carey, B. Sutherland, I. Hill, A. Amassian, H. Liu, J. Tang, O. M. Bakr and E. H. Sargent, *Nat. Mater.*, 2014, **13**, 822.
39 R. W. Crisp, D. M. Kroupa, A. R. Marshall, E. M. Miller, J. Zhang, M. C. Beard and J. M. Luther, *Sci. Rep.*, 2015, **5**, 9945.
40 I. J. Kramer, J. C. Minor, G. Moreno-Bautista, L. Rollny, P. Kanjanaboos, D. Kopilovic, S. M. Thon, G. H. Carey, K. W. Chou, D. Zhitomirsky, A. Amassian and E. H. Sargent, *Adv. Mater.*, 2015, **27**, 116–121.
41 Z. Yang, A. Janmohamed, X. Lan, F. P. García de Arquer, O. Voznyy, E. Yassitepe, G.-H. Kim, Z. Ning, X. Gong, R. Comin and E. H. Sargent, *Nano Lett.*, 2015, **15**, 7539–7543.
42 R. Azmi, H. Aqoma, W. T. Hadmojo, J.-M. Yun, S. Yoon, K. Kim, Y. R. Do, S.-H. Oh and S.-Y. Jang, *Adv. Energy Mater.*, 2016, **6**, 1502146.
43 R. Azmi, S.-H. Oh and S.-Y. Jang, *ACS Energy Lett.*, 2016, **1**, 100–106.
44 Y. Cao, A. Stavrinadis, T. Lasanta, D. So and G. Konstantatos, *Nat. Energy*, 2016, **1**, 16035.
45 Z. Jin, M. Yuan, H. Li, H. Yang, Q. Zhou, H. Liu, X. Lan, M. Liu, J. Wang, E. H. Sargent and Y. Li, *Adv. Funct. Mater.*, 2016, **26**, 5284–5289.
46 X. Lan, O. Voznyy, F. P. García de Arquer, M. Liu, J. Xu, A. H. Proppe, G. Walters, F. Fan, H. Tan, M. Liu, Z. Yang, S. Hoogland and E. H. Sargent, *Nano Lett.*, 2016, **16**, 4630–4634.
47 A. Swarnkar, A. R. Marshall, E. M. Sanehira, B. D. Chernomordik, D. T. Moore, J. A. Christians, T. Chakrabarti and J. M. Luther, *Science*, 2016, **354**, 92–95.
48 R. Azmi, S. Y. Nam, S. Sinaga, S.-H. Oh, T. K. Ahn, S. C. Yoon, I. H. Jung and S.-Y. Jang, *Nano Energy*, 2017, **39**, 355–362.
49 J. Choi, Y. Kim, J. W. Jo, J. Kim, B. Sun, G. Walters, F. P. García de Arquer, R. Quintero-Bermudez, Y. Li, C. S. Tan, L. N. Quan, A. P. T. Kam, S. Hoogland, Z. Lu, O. Voznyy and E. H. Sargent, *Adv. Mater.*, 2017, **29**, 1702350.
50 J. W. Jo, Y. Kim, J. Choi, F. P. G. de Arquer, G. Walters, B. Sun, O. Ouellette, J. Kim, A. H. Proppe, R. Quintero-Bermudez, J. Fan, J. Xu, C. S. Tan, O. Voznyy and E. H. Sargent, *Adv. Mater.*, 2017, **29**, 1703627.
51 A. Stavrinadis, S. Pradhan, P. Papagiorgis, G. Itskos and G. Konstantatos, *ACS Energy Lett.*, 2017, **2**, 739–744.
52 Z. Yang, J. Z. Fan, A. H. Proppe, F. P. G. d. Arquer, D. Rossouw, O. Voznyy, X. Lan, M. Liu, G. Walters, R. Quintero-Bermudez, B. Sun, S. Hoogland, G. A. Botton, S. O. Kelley and E. H. Sargent, *Nat. Commun.*, 2017, **8**, 1325.
53 X. Zhang, P. K. Santra, L. Tian, M. B. Johansson, H. Rensmo and E. M. J. Johansson, *ACS Nano*, 2017, **11**, 8478–8487.
54 E. M. Sanehira, A. R. Marshall, J. A. Christians, S. P. Harvey, P. N. Ciesielski, L. M. Wheeler, P. Schulz, L. Y. Lin, M. C. Beard and J. M. Luther, *Sci. Adv.*, 2017, **3**, eaao4204.
55 H. Aqoma and S.-Y. Jang, *Energy Environ. Sci.*, 2018, **11**, 1603–1609.
56 R. Azmi, G. Seo, T. K. Ahn and S.-Y. Jang, *ACS Appl. Mater. Interfaces*, 2018, **10**, 35244–35249.
57 S.-W. Baek, S.-H. Lee, J. H. Song, C. Kim, Y.-S. Ha, H. Shin, H. Kim, S. Jeong and J.-Y. Lee, *Energy Environ. Sci.*, 2018, **11**, 2078–2084.
58 L. Hu, Z. Zhang, R. J. Patterson, Y. Hu, W. Chen, C. Chen, D. Li, C. Hu, C. Ge, Z. Chen, L. Yuan, C. Yan, N. Song, Z. L. Teh, G. J. Conibeer, J. Tang and S. Huang, *Nano Energy*, 2018, **46**, 212–219.
59 J. Kim, O. Ouellette, O. Voznyy, M. Wei, J. Choi, M.-J. Choi, J. W. Jo, S.-W. Baek, J. Fan, M. I. Saidaminov, B. Sun, P. Li, D.-H. Nam, S. Hoogland, Z.-H. Lu, F. P. García de Arquer and E. H. Sargent, *Adv. Mater.*, 2018, **30**, 1803830.
60 K. Lu, Y. Wang, Z. Liu, L. Han, G. Shi, H. Fang, J. Chen, X. Ye, S. Chen, F. Yang, A. G. Shulga, T. Wu, M. Gu, S. Zhou, J. Fan, M. A. Loi and W. Ma, *Adv. Mater.*, 2018, **30**, 1707572.
61 Y. Wang, K. Lu, L. Han, Z. Liu, G. Shi, H. Fang, S. Chen, T. Wu, F. Yang, M. Gu, S. Zhou, X. Ling, X. Tang, J. Zheng, M. A. Loi and W. Ma, *Adv. Mater.*, 2018, **30**, 1704871.
62 J. Xu, O. Voznyy, M. Liu, A. R. Kirmani, G. Walters, R. Munir, M. Abdelsamie, A. H. Proppe, A. Sarkar,

F. P. García de Arquer, M. Wei, B. Sun, M. Liu, O. Ouellette, R. Quintero-Bermudez, J. Li, J. Fan, L. Quan, P. Todorovic, H. Tan, S. Hoogland, S. O. Kelley, M. Stefik, A. Amassian and E. H. Sargent, *Nat. Nanotechnol.*, 2018, **13**, 456–462.

63 Q. Wang, Z. Jin, D. Chen, D. Bai, H. Bian, J. Sun, G. Zhu, G. Wang and S. Liu, *Adv. Energy Mater.*, 2018, **8**, 1800007.

64 J. Yuan, X. Ling, D. Yang, F. Li, S. Zhou, J. Shi, Y. Qian, J. Hu, Y. Sun, Y. Yang, X. Gao, S. Duhm, Q. Zhang and W. Ma, *Joule*, 2018, **2**, 2450–2463.

65 L. Hu, X. Geng, S. Singh, J. Shi, Y. Hu, S. Li, X. Guan, T. He, X. Li, Z. Cheng, R. Patterson, S. Huang and T. Wu, *Nano Energy*, 2019, **64**, 103922.

66 X. Ling, S. Zhou, J. Yuan, J. Shi, Y. Qian, B. W. Larson, Q. Zhao, C. Qin, F. Li, G. Shi, C. Stewart, J. Hu, X. Zhang, J. M. Luther, S. Duhm and W. Ma, *Adv. Energy Mater.*, 2019, **9**, 1900721.

67 J. Shi, F. Li, J. Yuan, X. Ling, S. Zhou, Y. Qian and W. Ma, *J. Mater. Chem. A*, 2019, **7**, 20936–20944.

68 J. P. Clifford, K. W. Johnston, L. Levina and E. H. Sargent, *Appl. Phys. Lett.*, 2007, **91**, 253117.

69 C. Piliego, L. Protesescu, S. Z. Bisri, M. V. Kovalenko and M. A. Loi, *Energy Environ. Sci.*, 2013, **6**, 3054–3059.

70 M.-J. Choi, J. Oh, J.-K. Yoo, J. Choi, D. M. Sim and Y. S. Jung, *Energy Environ. Sci.*, 2014, **7**, 3052–3060.

71 J. Tang, X. Wang, L. Brzozowski, D. A. R. Barkhouse, R. Debnath, L. Levina and E. H. Sargent, *Adv. Mater.*, 2010, **22**, 1398–1402.

72 X.-D. Mai, H. J. An, J. H. Song, J. Jang, S. Kim and S. Jeong, *J. Mater. Chem. A*, 2014, **2**, 20799–20805.

73 M.-J. Choi, S. Kim, H. Lim, J. Choi, D. M. Sim, S. Yim, B. T. Ahn, J. Y. Kim and Y. S. Jung, *Adv. Mater.*, 2016, **28**, 1780–1787.

74 H. Lee, H. C. Leventis, S.-J. Moon, P. Chen, S. Ito, S. A. Haque, T. Torres, F. Nüesch, T. Geiger, S. M. Zakeeruddin, M. Grätzel and M. K. Nazeeruddin, *Adv. Funct. Mater.*, 2009, **19**, 2735–2742.

75 N. Zhao, T. P. Osedach, L.-Y. Chang, S. M. Geyer, D. Wanger, M. T. Binda, A. C. Arango, M. G. Bawendi and V. Bulovic, *ACS Nano*, 2010, **4**, 3743–3752.

76 S. M. Willis, C. Cheng, H. E. Assender and A. A. R. Watt, *Nano Lett.*, 2012, **12**, 1522–1526.

77 J. Jean, S. Chang, P. R. Brown, J. J. Cheng, P. H. Rekemeyer, M. G. Bawendi, S. Gradečak and V. Bulović, *Adv. Mater.*, 2013, **25**, 2790–2796.

78 S.-W. Baek, P. Molet, M.-J. Choi, M. Biondi, O. Ouellette, J. Fan, S. Hoogland, F. P. García de Arquer, A. Mihi and E. H. Sargent, *Adv. Mater.*, 1745, **0**, 190.

79 A. K. Rath, M. Bernechea, L. Martinez, F. P. G. de Arquer, J. Osmond and G. Konstantatos, *Nat. Photonics*, 2012, **6**, 529.

80 A. Stavrinadis, A. K. Rath, F. P. G. de Arquer, S. L. Diedenhofen, C. Magén, L. Martinez, D. So and G. Konstantatos, *Nat. Commun.*, 2013, **4**, 2981.

81 T. Zhao, E. D. Goodwin, J. Guo, H. Wang, B. T. Diroll, C. B. Murray and C. R. Kagan, *ACS Nano*, 2016, **10**, 9267–9273.

82 M. Yuan, D. Zhitomirsky, V. Adinolfi, O. Voznyy, K. W. Kemp, Z. Ning, X. Lan, J. Xu, J. Y. Kim, H. Dong and E. H. Sargent, *Adv. Mater.*, 2013, **25**, 5586–5592.

83 R. Wang, X. Wu, K. Xu, W. Zhou, Y. Shang, H. Tang, H. Chen and Z. Ning, *Adv. Mater.*, 2018, **30**, 1704882.

84 J. J. Choi, W. N. Wenger, R. S. Hoffman, Y.-F. Lim, J. Luria, J. Jasieniak, J. A. Marohn and T. Hanrath, *Adv. Mater.*, 2011, **23**, 3144–3148.

85 X. Wang, G. I. Koleilat, J. Tang, H. Liu, I. J. Kramer, R. Debnath, L. Brzozowski, D. A. R. Barkhouse, L. Levina, S. Hoogland and E. H. Sargent, *Nat. Photonics*, 2011, **5**, 480.

86 M. J. Speirs, B. G. H. M. Groeneveld, L. Protesescu, C. Piliego, M. V. Kovalenko and M. A. Loi, *Phys. Chem. Chem. Phys.*, 2014, **16**, 7672–7676.

87 T. Kim, Y. Gao, H. Hu, B. Yan, Z. Ning, L. K. Jagadamma, K. Zhao, A. R. Kirmani, J. Eid, M. M. Adachi, E. H. Sargent, P. M. Beaujuge and A. Amassian, *Nano Energy*, 2015, **17**, 196–205.

88 T. Kim, Y. Firdaus, A. R. Kirmani, R.-Z. Liang, H. Hu, M. Liu, A. El Labban, S. Hoogland, P. M. Beaujuge, E. H. Sargent and A. Amassian, *ACS Energy Lett.*, 2018, **3**, 1307–1314.

89 Y. Zhang, M. Gu, N. Li, Y. Xu, X. Ling, Y. Wang, S. Zhou, F. Li, F. Yang, K. Ji, J. Yuan and W. Ma, *J. Mater. Chem. A*, 2018, **6**, 24693–24701.

90 R. W. Crisp, G. F. Pach, J. M. Kurley, R. M. France, M. O. Reese, S. U. Nanayakkara, B. A. MacLeod, D. V. Talapin, M. C. Beard and J. M. Luther, *Nano Lett.*, 2017, **17**, 1020–1027.

91 G. Shi, Y. Wang, Z. Liu, L. Han, J. Liu, Y. Wang, K. Lu, S. Chen, X. Ling, Y. Li, S. Cheng and W. Ma, *Adv. Energy Mater.*, 2017, **7**, 1602667.

92 Y. Bi, S. Pradhan, M. Z. Akgul, S. Gupta, A. Stavrinadis, J. Wang and G. Konstantatos, *ACS Energy Lett.*, 2018, **3**, 1753–1759.

93 Y. Gao, J. Zheng, W. Chen, L. Yuan, Z. L. Teh, J. Yang, X. Cui, G. Conibeer, R. Patterson and S. Huang, *J. Phys. Chem. Lett.*, 2019, **10**, 5729–5734.

94 J. Kim, B. G. Jeong, H. Roh, J. Song, M. Park, D. C. Lee, W. K. Bae and C. Lee, *ACS Appl. Mater. Interfaces*, 2016, **8**, 23947–23952.

95 D. Mandal and A. K. Rath, *ACS Appl. Mater. Interfaces*, 2018, **10**, 39074–39082.

96 Q. A. Akkerman, M. Gandini, F. Di Stasio, P. Rastogi, F. Palazon, G. Bertoni, J. M. Ball, M. Prato, A. Petrozza and L. Manna, *Nat. Energy*, 2016, **2**, 16194.

97 F. Li, S. Zhou, J. Yuan, C. Qin, Y. Yang, J. Shi, X. Ling, Y. Li and W. Ma, *ACS Energy Lett.*, 2019, **4**, 2571–2578.

98 Q. Zhao, A. Hazarika, X. Chen, S. P. Harvey, B. W. Larson, G. R. Teeter, J. Liu, T. Song, C. Xiao, L. Shaw, M. Zhang, G. Li, M. C. Beard and J. M. Luther, *Nat. Commun.*, 2019, **10**, 2842.

99 R. Wang, Y. Shang, P. Kanjanaboos, W. Zhou, Z. Ning and E. H. Sargent, *Energy Environ. Sci.*, 2016, **9**, 1130–1143.

100 O. Voznyy, D. Zhitomirsky, P. Stadler, Z. Ning, S. Hoogland and E. H. Sargent, *ACS Nano*, 2012, **6**, 8448–8455.

101 M. Liu, O. Voznyy, R. Sabatini, F. P. García de Arquer, R. Munir, A. H. Balawi, X. Lan, F. Fan, G. Walters, A. R. Kirmani, S. Hoogland, F. Laquai, A. Amassian and E. H. Sargent, *Nat. Mater.*, 2016, **16**, 258.

102 B. Sun, O. Voznyy, H. Tan, P. Stadler, M. Liu, G. Walters, A. H. Proppe, M. Liu, J. Fan, T. Zhuang, J. Li, M. Wei, J. Xu,

Y. Kim, S. Hoogland and E. H. Sargent, *Adv. Mater.*, 2017, **29**, 1700749.
103 Y. Kim, F. Che, J. W. Jo, J. Choi, F. P. García de Arquer, O. Voznyy, B. Sun, J. Kim, M.-J. Choi, R. Quintero-Bermudez, F. Fan, C. S. Tan, E. Bladt, G. Walters, A. H. Proppe, C. Zou, H. Yuan, S. Bals, J. Hofkens, M. B. J. Roeffaers, S. Hoogland and E. H. Sargent, *Adv. Mater.*, 2019, **31**, 1805580.
104 H. Tavakoli Dastjerdi, D. Prochowicz, P. Yadav and M. M. Tavakoli, *Nanoscale*, 2019, **11**, 22832–22840.
105 H. Tavakoli Dastjerdi, R. Tavakoli, P. Yadav, D. Prochowicz, M. Saliba and M. M. Tavakoli, *ACS Appl. Mater. Interfaces*, 2019, **11**, 26047–26052.
106 B.-R. Hyun, J. J. Choi, K. L. Seyler, T. Hanrath and F. W. Wise, *ACS Nano*, 2013, **7**, 10938–10947.
107 B. F. Spencer, M. A. Leontiadou, P. C. J. Clark, A. I. Williamson, M. G. Silly, F. Sirotti, S. M. Fairclough, S. C. E. Tsang, D. C. J. Neo, H. E. Assender, A. A. R. Watt and W. R. Flavell, *Appl. Phys. Lett.*, 2016, **108**, 091603.
108 M. Yuan, O. Voznyy, D. Zhitomirsky, P. Kanjanaboos and E. H. Sargent, *Adv. Mater.*, 2015, **27**, 917–921.
109 R. L. Z. Hoye, B. Ehrler, M. L. Böhm, D. Muñoz-Rojas, R. M. Altamimi, A. Y. Alyamani, Y. Vaynzof, A. Sadhanala, G. Ercolano, N. C. Greenham, R. H. Friend, J. L. MacManus-Driscoll and K. P. Musselman, *Adv. Energy Mater.*, 2014, **4**, 1301544.
110 X. Zhang and E. M. J. Johansson, *J. Mater. Chem. A*, 2017, **5**, 303–310.
111 M. Liu, F. P. G. de Arquer, Y. Li, X. Lan, G.-H. Kim, O. Voznyy, L. K. Jagadamma, A. S. Abbas, S. Hoogland, Z. Lu, J. Y. Kim, A. Amassian and E. H. Sargent, *Adv. Mater.*, 2016, **28**, 4142–4148.
112 F. Yang, Y. Xu, M. Gu, S. Zhou, Y. Wang, K. Lu, Z. Liu, X. Ling, Z. Zhu, J. Chen, Z. Wu, Y. Zhang, Y. Xue, F. Li, J. Yuan and W. Ma, *J. Mater. Chem. A*, 2018, **6**, 17688–17697.
113 Y. Cho, P. Giraud, B. Hou, Y.-W. Lee, J. Hong, S. Lee, S. Pak, J. Lee, J. E. Jang, S. M. Morris, J. I. Sohn, S. Cha and J. M. Kim, *Adv. Energy Mater.*, 2018, **8**, 1700809.
114 M. M. Tavakoli, A. Simchi, Z. Fan and H. Aashuri, *Chem. Commun.*, 2016, **52**, 323–326.
115 C. Cheng, M. M. Lee, N. K. Noel, G. M. Hughes, J. M. Ball, H. E. Assender, H. J. Snaith and A. A. R. Watt, *ACS Appl. Mater. Interfaces*, 2014, **6**, 14247–14252.
116 H. Tavakoli Dastjerdi, D. Prochowic, P. Yadav and M. M. Tavakoli, *Sustainable Energy Fuels*, 2019, **3**, 3128–3134.
117 D.-K. Ko, P. R. Brown, M. G. Bawendi and V. Bulović, *Adv. Mater.*, 2014, **26**, 4845–4850.
118 H. Aqoma, M. A. Mubarok, W. Lee, W. T. Hadmojo, C. Park, T. K. Ahn, D. Y. Ryu and S.-Y. Jang, *Adv. Energy Mater.*, 2018, **8**, 1800572.
119 X. Zhang and E. M. J. Johansson, *Nano Energy*, 2016, **28**, 71–77.
120 R. A. Street and A. Salleo, *Appl. Phys. Lett.*, 2002, **81**, 2887–2889.
121 M. Stewart, R. S. Howell, L. Pires and M. K. Hatalis, *IEEE Trans. Electron Devices*, 2001, **48**, 845–851.
122 P. R. Brown, R. R. Lunt, N. Zhao, T. P. Osedach, D. D. Wanger, L.-Y. Chang, M. G. Bawendi and V. Bulović, *Nano Lett.*, 2011, **11**, 2955–2961.
123 S. M. Mahpeykar, Q. Xiong and X. Wang, *Opt. Express*, 2014, **22**, A1576–A1588.
124 X. Zhang, C. Hägglund, M. B. Johansson, K. Sveinbjörnsson and E. M. J. Johansson, *Adv. Funct. Mater.*, 2016, **26**, 1921–1929.
125 M. M. Tavakoli, M. Nasilowski, J. Zhao, M. G. Bawendi and J. Kong, *Small Methods*, 2019, **3**, 1900449.
126 W. Shockley and H. J. Queisser, *J. Appl. Phys.*, 1961, **32**, 510–519.
127 R. D. Schaller and V. I. Klimov, *Phys. Rev. Lett.*, 2004, **92**, 186601.
128 R. J. Ellingson, M. C. Beard, J. C. Johnson, P. Yu, O. I. Micic, A. J. Nozik, A. Shabaev and A. L. Efros, *Nano Lett.*, 2005, **5**, 865–871.
129 J. Tauc, *J. Phys. Chem. Solids*, 1959, **8**, 219–223.
130 S. Kolodinski, J. H. Werner, T. Wittchen and H. J. Queisser, *Appl. Phys. Lett.*, 1993, **63**, 2405–2407.
131 M. C. Beard, K. P. Knutsen, P. Yu, J. M. Luther, Q. Song, W. K. Metzger, R. J. Ellingson and A. J. Nozik, *Nano Lett.*, 2007, **7**, 2506–2512.
132 J. E. Murphy, M. C. Beard, A. G. Norman, S. P. Ahrenkiel, J. C. Johnson, P. Yu, O. I. Mićić, R. J. Ellingson and A. J. Nozik, *J. Am. Chem. Soc.*, 2006, **128**, 3241–3247.
133 R. D. Schaller, M. Sykora, S. Jeong and V. I. Klimov, *J. Phys. Chem. B*, 2006, **110**, 25332–25338.
134 A. Pandey and P. Guyot-Sionnest, *Science*, 2008, **322**, 929–932.
135 C. Delerue, G. Allan, J. J. H. Pijpers and M. Bonn, *Phys. Rev. B: Condens. Matter Mater. Phys.*, 2010, **81**, 125306.
136 A. J. Nozik, M. C. Beard, J. M. Luther, M. Law, R. J. Ellingson and J. C. Johnson, *Chem. Rev.*, 2010, **110**, 6873–6890.
137 V. I. Klimov, *Appl. Phys. Lett.*, 2006, **89**, 123118.
138 G. Nootz, L. A. Padilha, L. Levina, V. Sukhovatkin, S. Webster, L. Brzozowski, E. H. Sargent, D. J. Hagan and E. W. Van Stryland, *Phys. Rev. B: Condens. Matter Mater. Phys.*, 2011, **83**, 155302.
139 V. Sukhovatkin, S. Hinds, L. Brzozowski and E. H. Sargent, *Science*, 2009, **324**, 1542–1544.
140 N. J. L. K. Davis, M. L. Böhm, M. Tabachnyk, F. Wisnivesky-Rocca-Rivarola, T. C. Jellicoe, C. Ducati, B. Ehrler and N. C. Greenham, *Nat. Commun.*, 2015, **6**, 8259.
141 C. M. Cirloganu, L. A. Padilha, Q. Lin, N. S. Makarov, K. A. Velizhanin, H. Luo, I. Robel, J. M. Pietryga and V. I. Klimov, *Nat. Commun.*, 2014, **5**, 4148.
142 D. A. Quansah and M. S. Adaramola, *Renewable Energy*, 2019, **131**, 900–910.
143 S. Kim, A. R. Marshall, D. M. Kroupa, E. M. Miller, J. M. Luther, S. Jeong and M. C. Beard, *ACS Nano*, 2015, **9**, 8157–8164.
144 J. Chang, Y. Kuga, I. Mora-Seró, T. Toyoda, Y. Ogomi, S. Hayase, J. Bisquert and Q. Shen, *Nanoscale*, 2015, **7**, 5446–5456.
145 Y. Zhang, C. Ding, G. Wu, N. Nakazawa, J. Chang, Y. Ogomi, T. Toyoda, S. Hayase, K. Katayama and Q. Shen, *J. Phys. Chem. C*, 2016, **120**, 28509–28518.
146 X. Zhang, C. Hägglund and E. M. J. Johansson, *Energy Environ. Sci.*, 2017, **10**, 216–224.

147 X. Zhang, D. Jia, C. Hägglund, V. A. Öberg, J. Du, J. Liu and E. M. J. Johansson, *Nano Energy*, 2018, **53**, 373–382.
148 X. Zhang, J. Zhang, D. Phuyal, J. Du, L. Tian, V. A. Öberg, M. B. Johansson, U. B. Cappel, O. Karis, J. Liu, H. Rensmo, G. Boschloo and E. M. J. Johansson, *Adv. Energy Mater.*, 2018, **8**, 1702049.
149 W. Ahmad, J. He, Z. Liu, K. Xu, Z. Chen, X. Yang, D. Li, Y. Xia, J. Zhang and C. Chen, *Adv. Mater.*, 2019, **31**, 1900593.
150 J. Tang, L. Brzozowski, D. A. R. Barkhouse, X. Wang, R. Debnath, R. Wolowiec, E. Palmiano, L. Levina, A. G. Pattantyus-Abraham, D. Jamakosmanovic and E. H. Sargent, *ACS Nano*, 2010, **4**, 869–878.
151 S. Kim, S. H. Im, M. Kang, J. H. Heo, S. I. Seok, S.-W. Kim, I. Mora-Seró and J. Bisquert, *Phys. Chem. Chem. Phys.*, 2012, **14**, 14999–15002.
152 M. Sykora, A. Y. Koposov, J. A. McGuire, R. K. Schulze, O. Tretiak, J. M. Pietryga and V. I. Klimov, *ACS Nano*, 2010, **4**, 2021–2034.
153 J. W. Jo, J. Choi, F. P. García de Arquer, A. Seifitokaldani, B. Sun, Y. Kim, H. Ahn, J. Fan, R. Quintero-Bermudez, J. Kim, M.-J. Choi, S.-W. Baek, A. H. Proppe, G. Walters, D.-H. Nam, S. Kelley, S. Hoogland, O. Voznyy and E. H. Sargent, *Nano Lett.*, 2018, **18**, 4417–4423.
154 A. Rivaton, S. Chambon, M. Manceau, J.-L. Gardette, N. Lemaître and S. Guillerez, *Polym. Degrad. Stab.*, 2010, **95**, 278–284.
155 J. Razzell-Hollis, J. Wade, W. C. Tsoi, Y. Soon, J. Durrant and J.-S. Kim, *J. Mater. Chem. A*, 2014, **2**, 20189–20195.
156 F. A. Soria, E. M. Patrito and P. Paredes-Olivera, *J. Phys. Chem. C*, 2012, **116**, 24607–24615.
157 J. Kim, H. Jung, J. Song, K. Kim and C. Lee, *ACS Appl. Mater. Interfaces*, 2017, **9**, 24052–24060.
158 O. Pachoumi, C. Li, Y. Vaynzof, K. K. Banger and H. Sirringhaus, *Adv. Energy Mater.*, 2013, **3**, 1428–1436.
159 Q. An, P. Fassl, Y. J. Hofstetter, D. Becker-Koch, A. Bausch, P. E. Hopkinson and Y. Vaynzof, *Nano Energy*, 2017, **39**, 400–408.
160 S. Chen, Y. j. Wang, Q. Liu, G. Shi, Z. Liu, K. Lu, L. Han, X. Ling, H. Zhang, S. Cheng and W. Ma, *Adv. Energy Mater.*, 2018, **8**, 1701194.
161 W. Nie, J.-C. Blancon, A. J. Neukirch, K. Appavoo, H. Tsai, M. Chhowalla, M. A. Alam, M. Y. Sfeir, C. Katan, J. Even, S. Tretiak, J. J. Crochet, G. Gupta and A. D. Mohite, *Nat. Commun.*, 2016, **7**, 11574.
162 D. H. Webber and R. L. Brutchey, *J. Am. Chem. Soc.*, 2012, **134**, 1085–1092.
163 H. Zhao, H. Liang, B. A. Gonfa, M. Chaker, T. Ozaki, P. Tijssen, F. Vidal and D. Ma, *Nanoscale*, 2014, **6**, 215–225.
164 H. Zhao, M. Chaker, N. Wu and D. Ma, *J. Mater. Chem.*, 2011, **21**, 8898–8904.
165 A. Bansal and N. S. Lewis, *J. Phys. Chem. B*, 1998, **102**, 4058–4060.
166 J. M. Salazar-Rios, N. Sukharevska, M. J. Speirs, S. Jung, D. Dirin, R. M. Dragoman, S. Allard, M. V. Kovalenko, U. Scherf and M. A. Loi, *Adv. Mater. Interfaces*, 2018, **5**, 1801155.
167 Y. I. Lee, N. J. Jeon, B. J. Kim, H. Shim, T.-Y. Yang, S. I. Seok, J. Seo and S. G. Im, *Adv. Energy Mater.*, 2018, **8**, 1701928.
168 W. J. Baumgardner, K. Whitham and T. Hanrath, *Nano Lett.*, 2013, **13**, 3225–3231.
169 F. Giberti, M. Vörös and G. Galli, *Nano Lett.*, 2017, **17**, 2547–2553.
170 A. Fischer, L. Rollny, J. Pan, G. H. Carey, S. M. Thon, S. Hoogland, O. Voznyy, D. Zhitomirsky, J. Y. Kim, O. M. Bakr and E. H. Sargent, *Adv. Mater.*, 2013, **25**, 5742–5749.
171 I. J. Kramer, G. Moreno-Bautista, J. C. Minor, D. Kopilovic and E. H. Sargent, *Appl. Phys. Lett.*, 2014, **105**, 163902.
172 R. Quintero-Torres, C. A. Foell, J. Pichaandi, F. C. J. M. v. Veggel and J. F. Young, *Appl. Phys. Lett.*, 2012, **101**, 121904.
173 N. J. Jeon, J. H. Noh, Y. C. Kim, W. S. Yang, S. Ryu and S. I. Seok, *Nat. Mater.*, 2014, **13**, 897.
174 M. Eslamian and F. Zabihi, *Nanoscale Res. Lett.*, 2015, **10**, 462.
175 J. M. Luther, M. Law, Q. Song, C. L. Perkins, M. C. Beard and A. J. Nozik, *ACS Nano*, 2008, **2**, 271–280.
176 W. K. Bae, J. Joo, L. A. Padilha, J. Won, D. C. Lee, Q. Lin, W.-k. Koh, H. Luo, V. I. Klimov and J. M. Pietryga, *J. Am. Chem. Soc.*, 2012, **134**, 20160–20168.
177 Y. Liu, J. Tolentino, M. Gibbs, R. Ihly, C. L. Perkins, Y. Liu, N. Crawford, J. C. Hemminger and M. Law, *Nano Lett.*, 2013, **13**, 1578–1587.
178 J. L. Ellis, D. D. Hickstein, K. J. Schnitzenbaumer, M. B. Wilker, B. B. Palm, J. L. Jimenez, G. Dukovic, H. C. Kapteyn, M. M. Murnane and W. Xiong, *J. Am. Chem. Soc.*, 2015, **137**, 3759–3762.
179 T. Cassagneau, T. E. Mallouk and J. H. Fendler, *J. Am. Chem. Soc.*, 1998, **120**, 7848–7859.
180 N. J. Thompson, M. W. B. Wilson, D. N. Congreve, P. R. Brown, J. M. Scherer, T. S. Bischof, M. Wu, N. Geva, M. Welborn, T. V. Voorhis, V. Bulović, M. G. Bawendi and M. A. Baldo, *Nat. Mater.*, 2014, **13**, 1039.
181 Z. Jin, A. Wang, Q. Zhou, Y. Wang and J. Wang, *Sci. Rep.*, 2016, **6**, 37106.
182 H. Choi, J.-G. Lee, X. D. Mai, M. C. Beard, S. S. Yoon and S. Jeong, *Sci. Rep.*, 2017, **7**, 622.
183 C. Jiang, Z. Zhong, B. Liu, Z. He, J. Zou, L. Wang, J. Wang, J. Peng and Y. Cao, *ACS Appl. Mater. Interfaces*, 2016, **8**, 26162–26168.
184 T. M. Eggenhuisen, Y. Galagan, A. F. K. V. Biezemans, T. M. W. L. Slaats, W. P. Voorthuijzen, S. Kommeren, S. Shanmugam, J. P. Teunissen, A. Hadipour, W. J. H. Verhees, S. C. Veenstra, M. J. J. Coenen, J. Gilot, R. Andriessen and W. A. Groen, *J. Mater. Chem. A*, 2015, **3**, 7255–7262.
185 S. G. Hashmi, D. Martineau, X. Li, M. Ozkan, A. Tiihonen, M. I. Dar, T. Sarikka, S. M. Zakeeruddin, J. Paltakari, P. D. Lund and M. Grätzel, *Adv. Mater. Technol.*, 2017, **2**, 1600183.
186 X. Lin, R. Klenk, L. Wang, T. Köhler, J. Albert, S. Fiechter, A. Ennaoui and M. C. Lux-Steiner, *Energy Environ. Sci.*, 2016, **9**, 2037–2043.

187 W. Ji, S. Liu, H. Zhang, R. Wang, W. Xie and H. Zhang, *ACS Photonics*, 2017, **4**, 1271–1278.
188 K.-J. Chen, H.-C. Chen, K.-A. Tsai, C.-C. Lin, H.-H. Tsai, S.-H. Chien, B.-S. Cheng, Y.-J. Hsu, M.-H. Shih, C.-H. Tsai, H.-H. Shih and H.-C. Kuo, *Adv. Funct. Mater.*, 2012, **22**, 5138–5143.
189 H. Li, K. Wu, J. Lim, H.-J. Song and V. I. Klimov, *Nat. Energy*, 2016, **1**, 16157.
190 L. Wengeler, B. Schmidt-Hansberg, K. Peters, P. Scharfer and W. Schabel, *Chem. Eng. Process.*, 2011, **50**, 478–482.
191 M. O. Reese, S. Glynn, M. D. Kempe, D. L. McGott, M. S. Dabney, T. M. Barnes, S. Booth, D. Feldman and N. M. Haegel, *Nat. Energy*, 2018, **3**, 1002–1012.
192 J. Jean, J. Xiao, R. Nick, N. Moody, M. Nasilowski, M. Bawendi and V. Bulović, *Energy Environ. Sci.*, 2018, **11**, 2295–2305.
193 A. Karani, L. Yang, S. Bai, M. H. Futscher, H. J. Snaith, B. Ehrler, N. C. Greenham and D. Di, *ACS Energy Lett.*, 2018, **3**, 869–874.
194 http://www.iea-pvps.org/fileadmin/dam/public/report/statistics/2018_iea-pvps_report_2018.pdf.
195 Z. Huang, G. Zhai, Z. Zhang, C. Zhang, Y. Xia, L. Lian, X. Fu, D. Zhang and J. Zhang, *CrystEngComm*, 2017, **19**, 946–951.
196 http://pvinsights.com/, accessed on Dec. 10, 2019.
197 M. M. Lunardi, D. R. Needell, H. Bauser, M. Phelan, H. A. Atwater and R. Corkish, *Energy*, 2019, **181**, 1–10.
198 M. R. Bergren, N. S. Makarov, K. Ramasamy, A. Jackson, R. Guglielmetti and H. McDaniel, *ACS Energy Lett.*, 2018, **3**, 520–525.
199 H.-J. Song, B. G. Jeong, J. Lim, D. C. Lee, W. K. Bae and V. I. Klimov, *Nano Lett.*, 2018, **18**, 395–404.
200 C. A. Nelson, N. R. Monahan and X. Y. Zhu, *Energy Environ. Sci.*, 2013, **6**, 3508–3519.
201 X. Huang, S. Han, W. Huang and X. Liu, *Chem. Soc. Rev.*, 2013, **42**, 173–201.
202 B. S. Richards, *Sol. Energy Mater. Sol. Cells*, 2006, **90**, 2329–2337.
203 Y. Bi, S. Pradhan, S. Gupta, M. Z. Akgul, A. Stavrinadis and G. Konstantatos, *Adv. Mater.*, 2018, **30**, 1704928.
204 https://www.qdsolarinc.com/.
205 O. Ouellette, N. Hossain, B. R. Sutherland, A. Kiani, F. P. García de Arquer, H. Tan, M. Chaker, S. Hoogland and E. H. Sargent, *ACS Energy Lett.*, 2016, **1**, 852–857.
206 R. W. Crisp, N. Kirkwood, G. Grimaldi, S. Kinge, L. D. A. Siebbeles and A. J. Houtepen, *ACS Appl. Energy Mater.*, 2018, **1**, 6569–6576.
207 M. Bernechea, N. C. Miller, G. Xercavins, D. So, A. Stavrinadis and G. Konstantatos, *Nat. Photonics*, 2016, **10**, 521.
208 D. So, S. Pradhan and G. Konstantatos, *Nanoscale*, 2016, **8**, 16776–16785.
209 European Parliament, Council of the European Union, OJ 174 (European Parliament, Council of the European Union).
210 H.-J. Song, H. s. Yoon, Y. Ju, S. M. Kim, W. G. Shin, J. Lim, S. Ko, H. m. Hwang and G. H. Kang, *Sol. Energy*, 2019, **184**, 273–280.
211 D. Hahm, J. H. Chang, B. G. Jeong, P. Park, J. Kim, S. Lee, J. Choi, W. D. Kim, S. Rhee, J. Lim, D. C. Lee, C. Lee, K. Char and W. K. Bae, *Chem. Mater.*, 2019, **31**, 3476–3484.
212 J.-H. Kim and H. Yang, *Chem. Mater.*, 2016, **28**, 6329–6335.
213 J. Lim, M. Park, W. K. Bae, D. Lee, S. Lee, C. Lee and K. Char, *ACS Nano*, 2013, **7**, 9019–9026.
214 S. Adachi, *J. Appl. Phys.*, 1989, **66**, 6030–6040.
215 S. Tamang, S. Lee, H. Choi and S. Jeong, *Chem. Mater.*, 2016, **28**, 8119–8122.
216 W. Liu, J.-S. Lee and D. V. Talapin, *J. Am. Chem. Soc.*, 2013, **135**, 1349–1357.
217 R. D. Schaller, J. M. Pietryga and V. I. Klimov, *Nano Lett.*, 2007, **7**, 3469–3476.
218 Y.-H. Won, O. Cho, T. Kim, D.-Y. Chung, T. Kim, H. Chung, H. Jang, J. Lee, D. Kim and E. Jang, *Nature*, 2019, **575**, 634–638.
219 J. R. Heath, *Chem. Soc. Rev.*, 1998, **27**, 65–71.
220 D. Franke, D. K. Harris, O. Chen, O. T. Bruns, J. A. Carr, M. W. B. Wilson and M. G. Bawendi, *Nat. Commun.*, 2016, **7**, 12749.
221 J. H. Song, H. Choi, H. T. Pham and S. Jeong, *Nat. Commun.*, 2018, **9**, 4267.
222 S. Lin, Y. Feng, X. Wen, P. Zhang, S. Woo, S. Shrestha, G. Conibeer and S. Huang, *J. Phys. Chem. C*, 2015, **119**, 867–872.
223 T. Englman, E. Terkieltaub and L. Etgar, *J. Phys. Chem. C*, 2015, **119**, 12904–12909.
224 K. Li, S. Wang, C. Chen, R. Kondrotas, M. Hu, S. Lu, C. Wang, W. Chen and J. Tang, *J. Mater. Chem. A*, 2019, **7**, 9665–9672.
225 Z. Li, X. Liang, G. Li, H. Liu, H. Zhang, J. Guo, J. Chen, K. Shen, X. San, W. Yu, R. E. I. Schropp and Y. Mai, *Nat. Commun.*, 2019, **10**, 125.
226 I. Repins, M. A. Contreras, B. Egaas, C. DeHart, J. Scharf, C. L. Perkins, B. To and R. Noufi, *Prog. Photovoltaics*, 2008, **16**, 235–239.
227 J. Du, Z. Du, J.-S. Hu, Z. Pan, Q. Shen, J. Sun, D. Long, H. Dong, L. Sun, X. Zhong and L.-J. Wan, *J. Am. Chem. Soc.*, 2016, **138**, 4201–4209.
228 H. J. Yun, J. Lim, A. S. Fuhr, N. S. Makarov, S. Keene, M. Law, J. M. Pietryga and V. I. Klimov, *ACS Nano*, 2018, **12**, 12587–12596.
229 A. S. Fuhr, H. J. Yun, N. S. Makarov, H. Li, H. McDaniel and V. I. Klimov, *ACS Photonics*, 2017, **4**, 2425–2435.